Modelling of Three-Phase Flow Functions for Applications in Enhanced Oil Recovery

PhD Thesis

Randi Holm

Department of Mathematics
University of Bergen

February 2009

Preface

The work in this thesis has been done as a partial fulfilment for the degree Doctor of Philosophy in Applied Mathematics at the University of Bergen. The studies started in 2006 and have been a part of the project Enhanced Oil Recovery for Maximizing Tail Production supported by the Norwegian Research Council.

Professor Magne S. Espedal and Professor Arne Skauge have been my supervisors. Most of the work has been performed at the Centre for Integrated Petroleum Research (CIPR). From November 2007 to June 2008 I was visiting the Institute of Petroleum Engineering at the Heriot-Watt University in Scotland.

Acknowledgements

I would like to thank my supervisors Magne S. Espedal and Arne Skauge for helpful discussions and guidance. In addition, I would like to thank Erlend Øian and Bjørn-Ove Heimsund for advice in the start-up phase. A special thank to Roland Kaufmann for his contributions both related to research and computer assistance and for encouraging me along the way. Also, thanks to Johan Lie for reading the manuscript.

During my stay at the Heriot Watt University I was guided by Rink van Dijke and Sebastian Geiger. I want to thank them for sharing their knowledge and for giving me useful feedback.

I would also like to thank friends and colleagues at CIPR for a good research environment and company for lunch.

Contents

Part I

Overview and Background Material

Chapter 1

Introduction

Fossil fuel stored in reservoirs is an important source for energy. It takes millions of years to transform organic material into petroleum, which makes the resources non-renewable. The reserves are decreasing, but new technology makes it possible to recover larger amounts of the oil in place. To increase oil recovery, knowledge about the flow processes, together with a detailed description of the geology is important. It is possible to model fluid flow in the reservoir by mathematical and numerical models [7]. Thus, the effect of different production strategies can be estimated when planning the oil field.

Lately, water-alternating-gas (WAG) [27, 57, 81, 82] has been used to increase the oil recovery. In WAG, slugs of gas and water are injected sequentially. Because of the difference in density between gas and water, gas will recover oil towards the top of the reservoir, while water will recover the oil at the bottom. Then a larger fraction of the reservoir is swept by the injected phases, such that WAG leads to an improved sweep efficiency. Compared to pure injection of water or gas, WAG gives an increased oil recovery of typically $5 - 10$ percent of the initial oil in place [27, 82].

The model parameters can be categorised into rock properties and fluid properties [26]. The rock properties describe the geology, while the fluid properties describe water, oil and gas phases in the reservoir. The interactions between the different fluid phases and the fluid and the rock are described by flow functions. The flow functions depend on the phase saturations, but also on the history of the flow process itself. This leads to hysteresis effects, which means that the flow functions depend on the saturation history [26]. An accurate description of the model parameters and the the flow functions is necessary in order to estimate the behaviour in the reservoir.

Large heterogeneities in rock properties are challenging in flow modelling. As an example, fractures can change the flow pattern dramatically [47]. This is also a discretisation issue, because the reservoir should be discretised in a way that

makes it possible to implement the heterogeneities accurately. To model flow in fractured porous media, the mesh should fit the fractures to allow us to implement the correct rock properties along fractures.

Use of WAG leads to large regions of three-phase flow, where three-phase flow functions should be used to model flow accurately [29]. Three-phase flow functions are difficult to measure and existing empirical correlations [28, 86] are not precise. In addition, the fact that the flow functions are history-dependent increases the complexity. To get more knowledge about the flow functions, pore-scale models [14, 75, 91], which are based on the underlying pore-scale physics, are used. A capillary bundle model estimates consistent capillary pressure and relative permeability functions without hysteresis, while network models take hysteresis effects into consideration. The parameters in these models should be adjusted to the current field.

Three-phase capillary pressures can be predicted using a network model with parameters anchored such that experimentally measured two-phase flow functions are matched. This leads to a complex optimisation problem. Stochastic methods are useful for obtaining numerical solutions to problems which are too complicated to solve analytically. The Ensemble Kalman Filter is a sequential data assimilation method which is designed for large-scale filtering problems [37]. The method has a simple conceptual formulation and is relatively easy to implement.

In reservoir simulation physics, mathematics, reservoir engineering and computer programming are combined. Improving the mesh and the flow functions contribute to the primary goal of reservoir simulation, which is to predict future performance of a reservoir and optimise the recovery of hydrocarbons.

1.1 Petroleum Reservoirs

During millions of years under high pressure and high temperature organic material is transformed into crude oil and natural gas [89]. Dead plants and animals buried under kilometers of sand and mud have been decomposed by bacteria under pressure cooking. When the organic material is mixed with fine-grained sediments and buried, the hydrocarbons are preserved in a low-energy environment free of oxygen. Due to buoyancy these hydrocarbons migrate upwards from the source rock to a porous rock, following the path with less resistance. In the host rock the hydrocarbons are trapped by an impermeable layer. Without this impermeable layer the hydrocarbons will escape.

The hydrocarbons are stored in pores in the porous media, where they flow according to hydrodynamic laws. Because of the buoyancy effects, the least dense phase will be on top, such that gas is located above oil and water is located below. The porous media was originally filled with water, and because of trapping effects

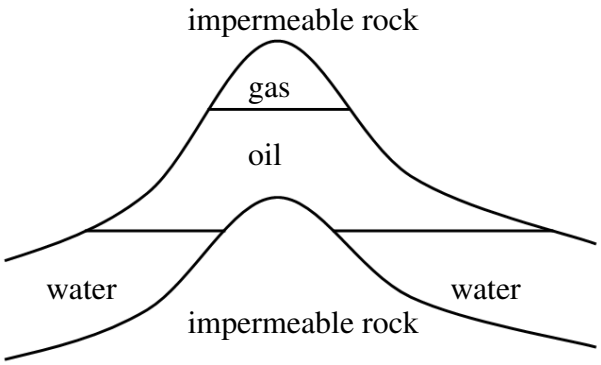

Figure 1.1: Hydrocarbon trap, where oil, gas and water are stored between impermeable layers.

some residual water may still be present in the upper parts of the reservoir. If the conditions in the reservoir change, the hydrocarbons move in order to reach a new equilibrium. Figure 1.1 shows a reservoir trap. Under the impermeable layer gas, oil and water are stored, respectively.

To bring oil and gas to the surface, wells are drilled. In the beginning of the production the pressure difference between the reservoir and the surface is high enough to be the driving force. This production is called primary recovery. The recovery factor for primary recovery varies from field to field, but usually about $25 - 30$ percent of the hydrocarbons are produced [74].

To maintain the pressure in the reservoir and displace more of the oil and gas, water can be injected into another well, leading hydrocarbons towards the production well. Methods where fluids are injected to increase the reservoir pressure are called secondary methods. With secondary recovery methods about 50 percent of the hydrocarbons are produced.

To displace oil located in small pores, a high pressure is necessary, because of capillary pressure effects. Since water is very mobile compared to oil, the water will follow the same path through the reservoir and not cover regions outside this path, such as small pores. Tertiary, or enhanced, recovery techniques try to modify fluid or rock properties to get a favourable effect on the production. One of the objectives is to achieve miscibility [26]. When there is no interface between oil and the injected fluid, capillary forces will not act. By increasing the temperature [3], the oil viscosity will decrease and oil will flow more easily. This will reduce the residual oil saturation. Injection of polymers [26] can clog pores, such that oil will flow in other pores than when secondary recovery methods are used. Tertiary methods are expensive, such that the ratio between the oil price and the injected

fluid is considered to estimate if there is an economic benefit.

1.2 Flow Functions

The relative permeability and capillary pressure are flow functions describing the interactions between fluids and rock when more than one phase is present [89]. The relative permeability is introduced through the multi-phase extension of Darcy's law and describes how well a fluid flows in presence of other fluids relative to if it was the only fluid present in the pores. The capillary pressure is the discontinuity of fluid pressure across an interface between two immiscible fluids.

The flow functions are complex and depend on the properties of both the fluids and the porous media. In practise, they are assumed to be functions of one or two phase saturations [26]. Hysteresis effects make the functions direction dependent, such that they can attain different values for one saturation state, depending on the history of the system. There are infinitely many saturation paths through the three-phase domain, which makes the hysteresis behaviour difficult to describe.

A good representation of flow functions is important in order to get a correct description of the fluid flow. Because of limited information about the functions, empirical functions depending on saturations [16, 17, 28, 67, 86, 87, 93] have been used. The functions typically include parameters for residual saturations and geometry of the porous media, which are chosen based on the available information. Usually the empirical functions are developed for water-wet reservoirs and do not reflect the behaviour in reservoirs with neutral to oil-wet wettability.

It is also common to use two-phase flow functions in three-phase flow simulations, because three-phase capillary pressures are difficult to measure experimentally. Using three-phase capillary pressure in simulations increases the three-phase zone considerably, and this leads to a higher oil production in the simulator [29].

In lack of reliable data, the capillary pressure is often neglected. When the capillary pressure is included in the simulation, the total oil production is considerably lower compared to when capillary pressure is neglected [29]. In addition, neglection of the capillary pressures leads to a reduced three-phase zone compared to when capillary pressures are included.

About half of the remaining oil reserves are located in carbonate reservoirs, which are often highly fractured [6]. The fractures have higher permeability than the matrix blocks between them, which means that the fractures give an important contribution to fluid flow. The fractures are dominated by viscous forces, while the rest of the reservoir is dominated by capillary forces. Typically, the oil is held back in the low-permeability matrix, where the flow velocity is low, resulting in an average oil recovery of only 30 percent worldwide. To improve the recovery, enhanced oil recovery (EOR) techniques, such as WAG, chemical injection [6]

and thermal recovery [3], are relevant. These techniques can lead to modified wettability and large three-phase flow regions. Approximately 90 percent of the carbonate reservoirs are neutral to oil-wet, such that three-phase flow functions for this wettability are necessary in flow simulations of the heterogeneous carbonate reservoirs.

Chapter 2

From Pore-Scale to Reservoir-Scale

To predict fluid flow in a reservoir, a mathematical model is used to estimate state variables. Both the equations and the variables must be defined on a scale that provides us with the information we want [47]. Fluid flow simulations on a molecular level are impossible to perform due to the large number of molecules. Also with a pore-scale perspective the number of unknowns is too large. Moreover, the geometry is complex and we do not have accurate knowledge about it, since the geology of the subsurface cannot be examined directly. On the reservoir-scale different equations and variables are obtained to describe the behaviour of fluid phases as continua. The pore-scale processes can not be described by these variables, but we aim at reflecting the effect of the pore-sale processes on the reservoir scale.

The detailed description of geometry on the pore-scale is replaced by averaged variables, such as porosity and permeability [47]. Instead of a description of where different fluids and the interfaces between them are, fluid saturations are introduced. Similarly, the relations between the fluids, described by interfacial tensions and contact angles on the pore-scale, are replaced by capillary pressure and relative permeability.

The new variables describe averaged properties over a representative elementary volume (REV), chosen such that fluctuations on micro-scale are smoothed out and macro-scale heterogeneities are preserved [47]. Figure 2.1 shows the porosity averaged over different volumes. If the representative elementary volume is very small, it may contain only cavity or solid, corresponding to porosity equal to one or zero, respectively. As the volume increases the porosity is averaged over larger volumes and the fluctuations decrease. If the representative elementary volume is too large, large-scale heterogeneities cause new fluctuations. An averaging

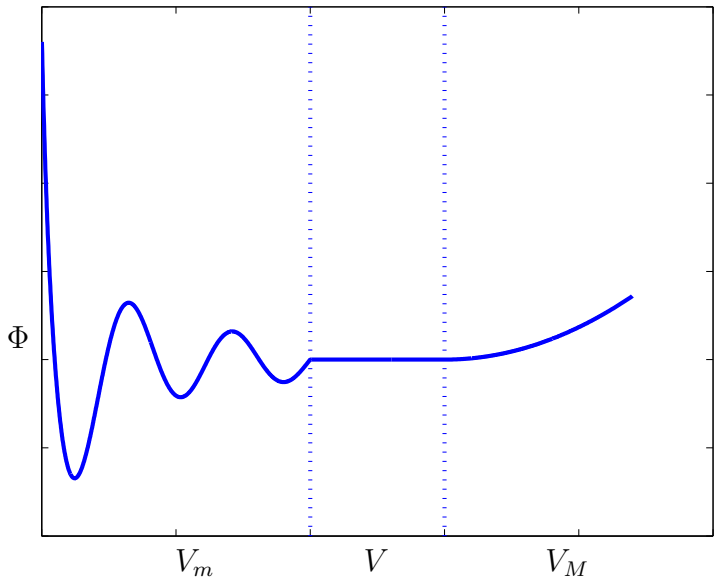

Figure 2.1: Porosity Φ averaged over different volumes. A small volume V_m causes fluctuations, while a large volume V_M is affected by large-scale heterogeneities. A representative elementary volume V should be of size $V_m << V << V_M$.

volume V should therefore satisfy [47]

$$V_m << V << V_M, \tag{2.1}$$

where V_m is a pore-scale volume and V_M is a large-scale volume. When this condition is satisfied, the averaging value is representative for the property it describes.

To understand the behaviour on the reservoir-scale, the pore-scale model is useful. Therefore, we start by describing the pore-scale properties, before the reservoir-scale properties are introduced.

2.1 Pore-scale properties

On the pore-scale interfacial tensions describe the relations between fluids. The wettability describes the behaviour of the fluids in contact with a solid surface and is given as contact angles. Capillary pressures are found from the Young-Laplace equation [47].

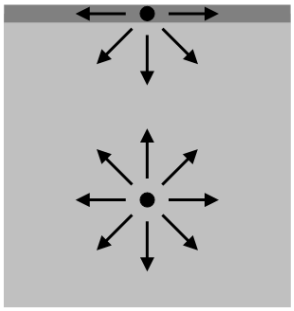

Figure 2.2: Cohesive forces between molecules in a liquid. A molecule away from the surface is attracted to neighbouring molecules in all directions, while a molecule at the surface is only surrounded by molecules half way around and is therefore subject to a net force directed toward the bulk volume. The surface will act like a membrane, which resists change.

2.1.1 Interfacial tensions

Two immiscible liquids in contact are separated by an interface, where interfacial tensions act. The interfacial tension is the work W per unit area A required to increase the interface [60]

$$\sigma = \frac{dW}{dA}. \tag{2.2}$$

If one of the liquids is a gas, the term surface tension is often used instead of interfacial tension.

Within a liquid attractive forces, called Van der Waals forces, act between the molecules. A molecule inside a liquid is surrounded by other molecules on all sides and is pulled equally in all directions. A molecule at the interface is attracted to the internal molecules, while the outward attraction depends on the surrounding fluid. This imbalance in forces makes the interface behave like a membrane, which tries to minimise its area and resist change [32].

Spreading coefficients

When three phases coexist different configurations occur, depending on the interfacial tensions between the phases. The configuration is described by the spreading coefficient, which is defined as the imbalance of forces when a fluid spreads

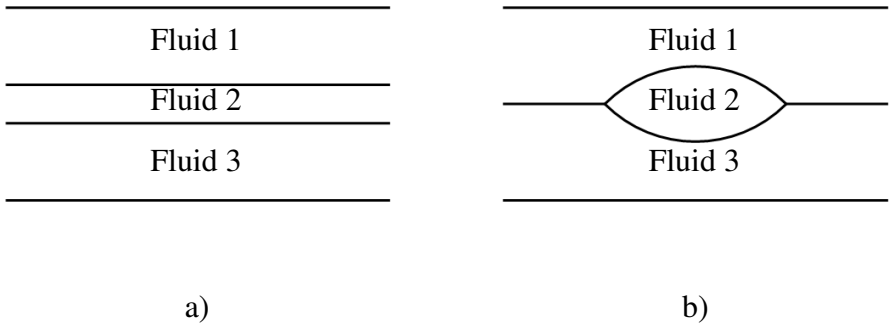

Figure 2.3: a) A spreading system, and b) a non-spreading system.

on a solid or on the surface of another immiscible fluid [85]. The spreading coefficients for water, oil and gas, respectively, are defined as

$$\begin{aligned} C_{s,w} &= \sigma_{go} - \sigma_{gw} - \sigma_{ow}, \\ C_{s,o} &= \sigma_{gw} - \sigma_{ow} - \sigma_{go}, \\ C_{s,g} &= \sigma_{ow} - \sigma_{gw} - \sigma_{go}, \end{aligned} \tag{2.3}$$

where σ_{ij} is the interfacial tension between phases i and j. If the spreading coefficient for a phase is non-negative, the phase will form a spreading layer between the other two phases, as shown in Figure 2.3a). If all spreading coefficients are negative, a three-phase contact is formed between the fluids and the system is non-spreading, as shown in Figure 2.3b).

2.1.2 Wettability

The wettability describes how two fluids behave in contact with a solid surface. The interface between the fluids meets the solid surface at a contact angle θ, measured through the most dens phase by convention. Fluids have different ability to wet a surface, as shown in Figure 2.4. For a wetting fluid $\theta < 90^\circ$ and for a non-wetting fluid $\theta > 90^\circ$. If $\theta = 90^\circ$, the two phases are equally wetting relative to each other. Interfacial tensions and wettability are connected, since the contact angle is the angle the interfacial tension between two fluids make with a solid.

Usually the cosine to the contact angle is used to describe the wettability. Thus, the wettability is water-wet if $0 < \cos\theta_{ow} \leq 1$ and oil-wet if $-1 \leq \cos\theta_{ow} < 0$. The concepts strongly water-wet and oil-wet are used if $\cos\theta_{ow}$ is close to the extreme values, which are 1 and -1, respectively. Similarly, the wettability is weakly water-wet or oil-wet if $\cos\theta_{ow}$ is close to 0.

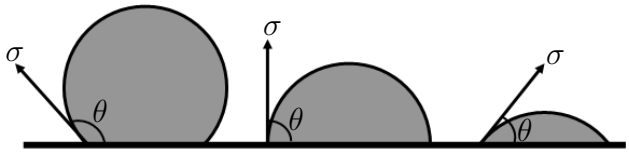

Figure 2.4: The drop to the left is non-wetting, the drop in the middle is neutrally wetting and the drop to the right is wetting.

The wettability can also be described with a contact angle distribution, where $\cos\theta_{ow}$ is distributed between a lower and an upper value, possibly varying with the radius of the pores. For mixed-wet large (MWL) wettability small pores are water-wet and large pores are oil-wet. The opposite is mixed-wet-small (MWS), where small pores are oil-wet and large pores are water-wet. If the wettability distribution consists of scattered regions, the wettability is fractional [89].

If a rock is filled with a phase over a long period of time, the wettability is influenced by this phase [89]. It is assumed that all petroleum reservoirs originally were filled with water, such that the wettability was water-wet. When oil gradually migrated into the reservoirs, the wettability in oil-filled pores changed towards oil-wet. In a water-wet medium oil starts to displace water in the largest pores, such oil is located in the large pores and water is located in the small pores. Therefore the wettability in petroleum reservoirs is often assumed to be mixed-wet large.

Bartell-Osterhof equation

The Bartell-Osterhof equation [9] describes the relationship between contact angles and interfacial tensions for three different phases. The equation can be derived by considering three systems with two phases and a solid in equilibrium. This is illustrated in Figure 2.5, where the interfacial tensions between two phases and a solid are shown for three different systems.

In the horizontal direction, the relationship between the interfacial tensions can be expressed as a scalar equation by using the contact angle θ_{ow} between oil and water

$$\sigma_{ow}\cos\theta_{ow} = \sigma_{os} - \sigma_{ws}, \tag{2.4}$$

where σ_{ow} is the interfacial tension between oil and water, σ_{os} is the interfacial tension between oil and solid, and σ_{ws} is the interfacial tension between water

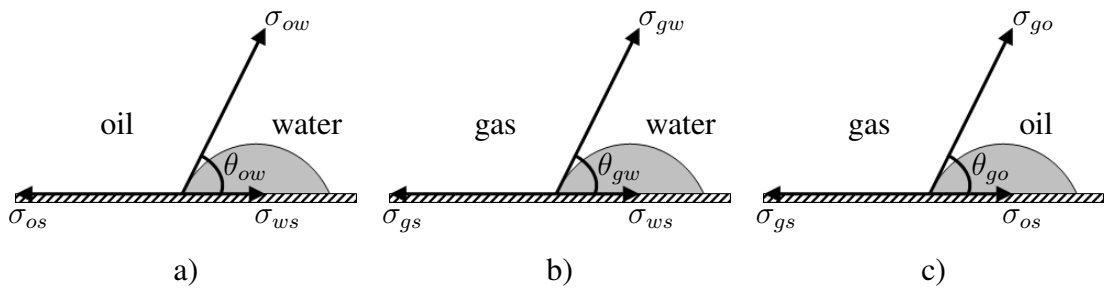

Figure 2.5: For a system in equilibrium the interfacial tensions must balance in the intersection point. a) A system with oil and water. b) A system with gas and water. c) A system with gas and oil.

and solid. A similar relationship can be expressed by using the contact angle θ_{gw} between gas and water,

$$\sigma_{gw} \cos \theta_{gw} = \sigma_{gs} - \sigma_{ws}, \tag{2.5}$$

where σ_{gw} is the interfacial tension between gas and water and σ_{gs} is the interfacial tension between gas and solid, or by using the contact angle θ_{go} between gas and oil,

$$\sigma_{go} \cos \theta_{go} = \sigma_{gs} - \sigma_{os}, \tag{2.6}$$

where σ_{go} is the interfacial tension between gas and oil. By eliminating the fluid-solid interfacial tensions we get the Bartell-Osterhof equation,

$$\sigma_{gw} \cos \theta_{gw} = \sigma_{go} \cos \theta_{go} + \sigma_{ow} \cos \theta_{ow}. \tag{2.7}$$

Linear relationship between contact angles

The cosines of the gas-oil contact angle $\cos \theta_{go}$ and of the gas-water contact angle $\cos \theta_{gw}$ are linked linearly to $\cos \theta_{ow}$ [85] by

$$\begin{aligned} \cos \theta_{go} &= \frac{1}{2\sigma_{go}}(C'_{s,o} \cos \theta_{ow} + C'_{s,o} + 2\sigma_{go}), \\ \cos \theta_{gw} &= \frac{1}{2\sigma_{gw}}((C'_{s,o} + 2\sigma_{ow}) \cos \theta_{ow} + C'_{s,o} + 2\sigma_{go}), \end{aligned} \tag{2.8}$$

where $C'_{s,o}$ is

$$C'_{s,o} = \min(0, C_{s,o}). \tag{2.9}$$

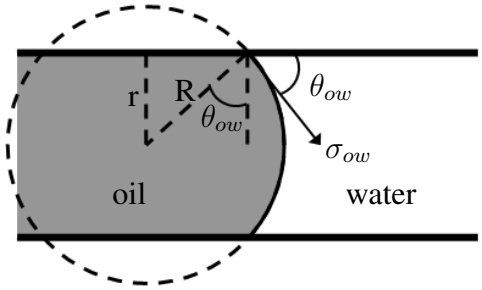

Figure 2.6: Two fluids inside a cylindrical tube with radius r. The interface between the fluids are described by the radius R and make the angle θ_{ow} with the pore wall.

2.1.3 Young-Laplace equation

The capillary pressure is the difference in pressure between two immiscible fluids at equilibrium and is a consequence of the interfacial tensions at the interface. Under the assumption that the fluids are in static equilibrium, the capillary pressure can be found by the Young-Laplace equation [56, 100]

$$P_c = \sigma(\frac{1}{R_x} + \frac{1}{R_y}), \tag{2.10}$$

where R_x and R_y are two arbitrary orthogonal radii of curvature [89]. By the Euler Theorem assertion [66] we know that the expression $\frac{1}{R_x} + \frac{1}{R_y}$ is constant for all orthogonal radii of curvature. To simplify the expression we define the mean radius of curvature by the harmonic mean of the R_x and R_y

$$\frac{1}{R} = \frac{1}{2}\left(\frac{1}{R_x} + \frac{1}{R_y}\right). \tag{2.11}$$

If the surface is spherical, the mean radius of curvature will equal the two orthogonal radii. By using the mean curvature the capillary pressure is expressed as

$$P_c = \frac{2\sigma}{R}. \tag{2.12}$$

The relation between the radius of curvature R and the radius r of a capillary tube is

$$R = \frac{r}{\cos\theta}, \tag{2.13}$$

as illustrated in Figure 2.6. The capillary pressure therefore depends on both the pore space, represented by the radius r, and the chemical structure of the fluids and the solid, described by θ and σ. For a cylindrical pore with radius r the capillary entry condition is

$$P_c = \frac{2\sigma \cos\theta}{r}. \tag{2.14}$$

If the fluids are not in equilibrium, Eq. (2.14) is not fulfilled. To reestablish the equilibrium fluids will start to flow through the pores. In a two-phase scenario oil displaces water if

$$P_{ow} > P_{c,ow}, \tag{2.15}$$

and water will displace oil if

$$P_{ow} < P_{c,ow}. \tag{2.16}$$

where P_{ij} is the pressure difference between phases i and j. When three phases are present two inequalities must be fulfilled for each phase displacement. A pore will be water-filled if

$$\begin{aligned} P_{gw} &< P_{c,gw}, \\ P_{ow} &< P_{c,ow}, \end{aligned} \tag{2.17}$$

oil-filled if

$$\begin{aligned} P_{go} &< P_{c,go}, \\ P_{ow} &> P_{c,ow}, \end{aligned} \tag{2.18}$$

and gas-filled if

$$\begin{aligned} P_{go} &> P_{c,go}, \\ P_{gw} &> P_{c,gw}. \end{aligned} \tag{2.19}$$

2.1.4 Hysteresis

In a capillary tube the phase occupancy depends on constant radius, contact angle and interfacial tensions. In more complicated models interfacial tensions and contact angles may change depending on which direction the fluids are flowing. In a network of connected pores, trapping of phases is introduced. This results in hysteresis effects for the capillary pressure and relative permeability functions on the reservoir-scale. Thus, in addition to the current state of the system the flow functions depend on the history of states.

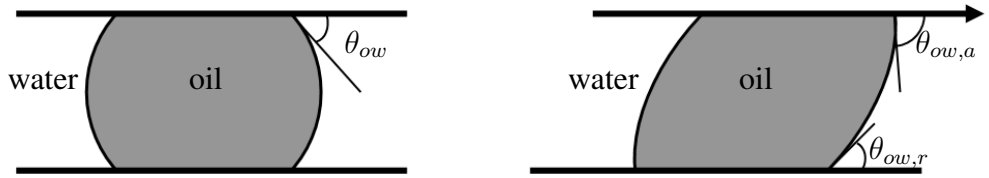

a) b)

Figure 2.7: An oil drop between two horizontal plates. a) The oil drop is in equilibrium. b) By moving the plate on top, advancing and receding contact angles are created. The advancing contact angle is larger than the receding, such that $\theta_{ow,a} > \theta_{ow,r}$.

Contact angle hysteresis

When a drop is in motion, the contact angles depend on the direction of the movement. The advancing contact angle is larger that the contact angle for the drop in equilibrium, while the receding contact angle is smaller.

Snap-off

Snap-off is another type of displacement. If the invading fluid is the wetting phase, it can flow through films along the pore wall, as shown in Figure 2.8. The thickness of the films increase in size until it snaps off the non-wetting phase and fills the whole pore. Snap-off occurs when the pressure difference between the phases is half the value of the capillary entry pressure given by the Young-Laplace equation [85]. After snap-off parts of the non-wetting phase are no longer connected to the rest of the non-wetting phase. This can lead to trapping, and the trapped phase can not escape unless it is re-connected to the rest of the non-wetting phase.

Pore-Doublet model

The Pore-Doublet model explains a different type of trapping. In a network of pores a phase can disconnect from the rest of the phase because of different fluid velocities through pores of different sizes [24]. The fluid velocity is governed by the relationship between the capillary and viscous forces, which depends on the

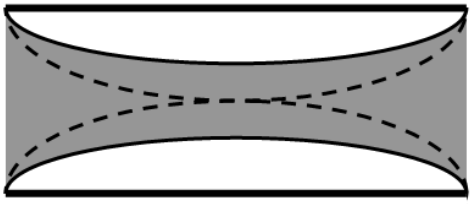

Figure 2.8: The wetting phase (white) forms a film close to the pore wall. As the film increases in size, it snaps off the non-wetting phase (grey) and fills the whole pore. This leads to trapping of the non-wetting phase.

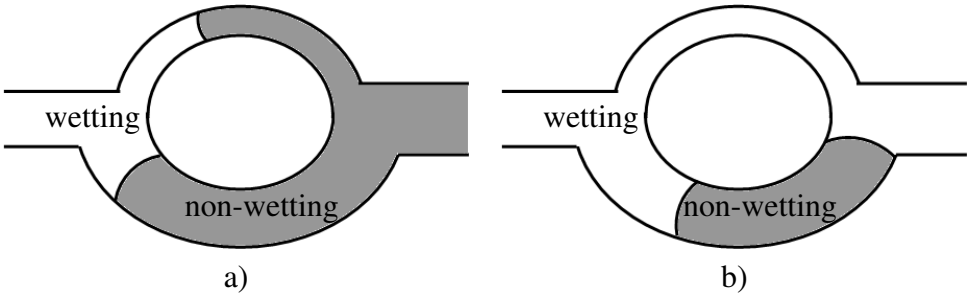

Figure 2.9: a) The velocity is higher in the small pore, resulting in b) trapping of the non-wetting phase in the large pore.

size of the pore. This is illustrated in Figure 2.9, where the non-wetting phase is trapped in the large pore because of higher flow velocity in the small pore.

2.2 Reservoir-scale properties

On the macro-scale new variables are defined within a representative elementary volume. The rock properties are described by porosity and permeability, while the fluids are described by density, viscosity and saturations. Relative permeability and capillary pressure are flow functions which depend on both the rock and fluid properties.

Accurate knowledge of rock and fluid properties is required for efficient development, management and prediction of future performance of the oilfield.

2.2.1 Rock properties

Petroleum is located in sedimentary rocks accumulated by rivers and oceans over a long time. The flow transports small particles, like clean granular material, silt, clay and organic material, which eventually settles on the seafloor. The particles have different size, shape and density, and therefore flow with different velocities. This leads to a sorting of the particles, with small particles settling in one area and larger particles in other areas. Changes in the climatic conditions cause variation in the assortment of particles, such that layers of different particles are formed. Later, the layers have been sealed with impermeable cap rocks [89], compressed and folded due to movements in the crust.

Rocks are porous and consist of solid with cavities that can contain fluids. A cavity is either isolated from or connected to other cavities. Fluids can only flow through the connected pores, such that the isolated pores do not contribute to transport. The effective porosity of a rock is given as [89]

$$\phi = \frac{V_p}{V_B}, \tag{2.20}$$

where V_p is the connected pore volume and V_B is the total volume of the rock. In petroleum reservoirs porosities between 0.1 and 0.2 occur most frequently [7]. In general, coarse sandstones with grains of uniform size have higher porosity than stones where smaller particles are mixed in. Porosity can depend on pressure and temperature, but this is usually negligible.

The absolute permeability K describes the ability of the rock to transmit fluids through its interconnected pores. Size, shape and packing of the grains in the rock are important factors, as well as consolidation and cementation. Depending on the shape of the grains, permeability can be different in different directions. The permeability is called anisotropic if permeability depends on flow direction. A reservoir typically consists of layers with different rock types. If the reservoir is inhomogeneous with respect to rock types, the permeability depends on spacial variables, $K(x, y, z)$. The unit for permeability is Darcy (D). A medium with a permeability of 1 Darcy permits a fluid with viscosity 1 cP (1 mPas) to flow with velocity 1 cm/s under a pressure gradient of 1 atm/cm [74]. The permeability for a rock is considered as good if it is larger than 50 mD.

Natural stress on the rock can cause fractures, which are visible as discontinuities in the rock. Fractures can act as barriers or conduits for fluid flow and causes significant variation in the distribution of porosity and permeability in the reservoir [63]. They are therefore important factors for determining flow paths [72].

2.2.2 Fluid properties

The saturation of a phase is the fraction of pore volume in a porous media occupied by a given phase α [89]

$$S_\alpha = \frac{V_\alpha}{V_p}, \tag{2.21}$$

where V_α is the volume filled with phase α and V_p is the pore volume. The pores are fully saturated, such that

$$\sum_{\alpha=1}^{n} S_\alpha = 1, \tag{2.22}$$

where n is the number of phases. This also implies that

$$\sum_{\alpha=1}^{n} V_\alpha = V_p, \tag{2.23}$$

where V_α is the volume of phase α.

Viscosity measures a fluid's internal resistance to flow, and a fluid with high viscosity flows more easily than a fluid with low viscosity. The unit for viscosity is Pa·s. Also poise (P) is used, and 1 Pa·s equals 10 P.

2.2.3 Darcy's law

The ability to transmit fluid is empirically described with Darcy's law. The engineer Henry Darcy performed experiments with flow of water through beds of sand. He discovered that the average velocity for the water was proportional to the pressure gradient, flowing from high to low pressure. The Darcy velocity is based on the time a particle uses to travel a given distance, and is therefore smaller than the real velocity a particle has in the pores, since pores are not straight.

Darcy's law for single phase flow is [31]

$$u = \frac{q}{A} = -\frac{K}{\mu}\frac{dp}{dx}, \tag{2.24}$$

where q is the flow rate, A is the cross-sectional area of the rock, K is the absolute permeability, μ is the viscosity and $\frac{dp}{dx}$ is the pressure gradient. It is only valid if the flow is laminar, the velocity is small and the friction between fluid and pores is large.

When several immiscible fluids are present in a rock, they interact with each other. The phases then flow with a reduced effective permeability, described by the relative permeability $k_{r,\alpha}$. The capillary pressure is introduced to describe

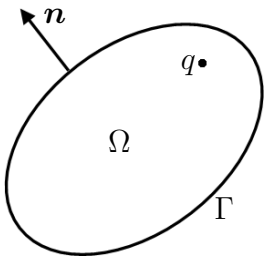

Figure 2.10: A control volume Ω with surface Γ and outward normal vector $\boldsymbol{n}$.

the relation between the phase pressures p_α. Both the relative permeability and capillary pressure are functions of saturations, and will be described in Section 2.2.6.

For immiscible multiphase flow the Darcy velocity for phase α is given by [68, 78]

$$u_\alpha = -K\lambda_\alpha \frac{dp_\alpha}{dx}, \tag{2.25}$$

where

$$\lambda_\alpha = \frac{k_{r,\alpha}}{\mu_\alpha} \tag{2.26}$$

is the mobility of phase α. Extending Darcy's law to three dimensions and including gravity yields

$$\boldsymbol{u}_\alpha = -\boldsymbol{K}\lambda_\alpha(\nabla p_\alpha - \rho \boldsymbol{g}), \tag{2.27}$$

where $\boldsymbol{g}$ is the gravity and the absolute permeability $\boldsymbol{K}$ is now a matrix.

2.2.4 Conservation laws

Consider the quantity u inside a volume Ω with boundary Γ and outward normal vector $\boldsymbol{n}$, shown in Figure 2.10. The change in u inside Ω is caused by the flux $\boldsymbol{F}$ over the boundary and the amount q generated within Ω. On the integral form, the conservation of u is expressed as [35]

$$\int_\Omega \frac{\partial u}{\partial t} dV + \int_\Gamma \boldsymbol{F} \cdot \boldsymbol{n} dS = \int_\Omega q dV, \tag{2.28}$$

where q is positive for sources and negative for sinks. Using Gauss' divergence theorem [35] the boundary flux integral can be converted into a volume integral, resulting in the equation

$$\int_\Omega (\frac{\partial u}{\partial t} + \nabla \cdot \boldsymbol{F} - q) dV = 0. \tag{2.29}$$

Since this holds for any volume Ω, it will also hold without the integral sign. This leads to the conservation law in differential form

$$\frac{\partial u}{\partial t} + \nabla \cdot \boldsymbol{F} = q. \tag{2.30}$$

For a porous medium the quantity u equals ϕS_α, where α denotes the phase, and the flux $\boldsymbol{F}$ equals $\boldsymbol{K}\boldsymbol{u}_\alpha$, where $\boldsymbol{u}_\alpha$ is given by Darcy's law (Eq. (2.27)). In three-phase flow the conservation law for phase α is given by

$$\frac{\partial}{\partial t}(\phi S_\alpha) - \nabla \cdot (\boldsymbol{K}\lambda_\alpha \nabla p_\alpha) = q_\alpha, \qquad \text{for } \alpha = w, o, g, \tag{2.31}$$

where the phase saturations satisfy

$$\sum_\alpha S_\alpha = 1, \tag{2.32}$$

and the phase pressures are linked by capillary pressures

$$\begin{aligned} p_o &= p_w + P_{c,ow}, \\ p_g &= p_w + P_{c,ow} + P_{c,go}. \end{aligned} \tag{2.33}$$

This constitutes a set of six equations, which can be solved for the six unknowns S_w, S_o, S_g, p_w, p_o and p_g. The behaviour of the equations depends on the form of the capillary pressure and relative permeability functions.

The conservation law describes how fluids flow in a porous medium and is therefore a cornerstone in reservoir modelling. In general, Eqs. (2.31), (2.32) and (2.33) can not be solved analytically, because of their highly non-linear nature. Instead, numerical methods are used to find solutions for discrete times at discrete points in the reservoir. To do this, it is necessary to make a discretisation of the domain.

2.2.5 Discretisation

To model fluid flow the reservoir is divided into cells, which are assigned rock properties and initial values for state variables. This allows us to approximate the flow equations by algebraic equations that can be solved in each cell.

Heterogeneities, such as fractures, may have a strong influence on the flow pattern. Therefore, it is important that the discretisation represents the geometry of the heterogeneities. Using unstructured triangular grids it is possible to capture the geometry in complex geological systems. Equilateral triangles are beneficial for a finite volume discretisation, as fluid flow between elements of very different size is only possible at small time steps. Often good geometrical fitting leads to

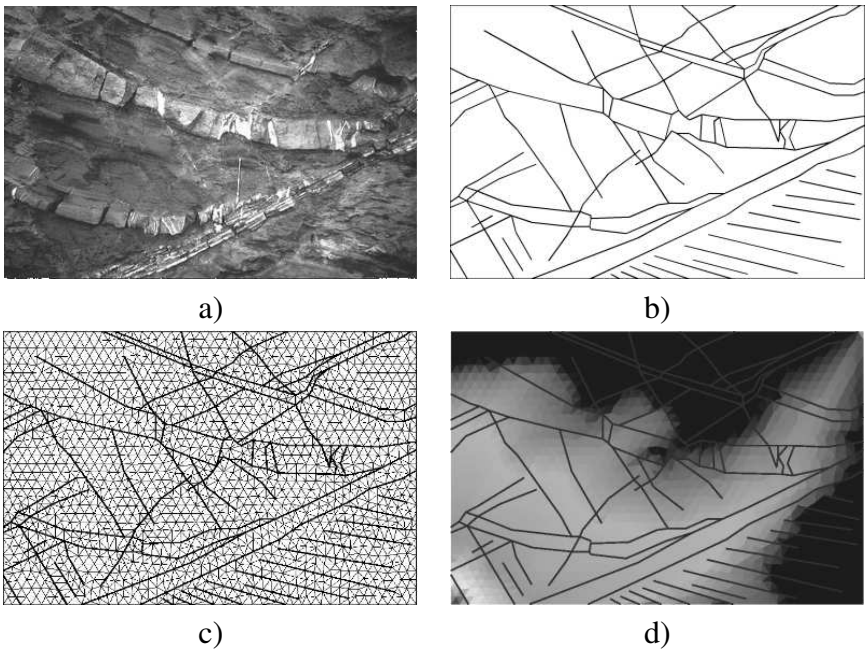

Figure 2.11: a) A photograph of a meter scale outcrop. b) The corresponding bitmap of manually interpreted layers and fractures/deformation bands. c) A mesh with about 5600 triangles. d) Water saturation after injecting water in the lower left corner and producing oil from the upper right corner.

triangles that are far from equilateral, and it is a challenge to create a mesh with both good geometry adaption and element shape.

Figure 2.11a) shows a meter scale outcrop with strong heterogeneities, while Figure 2.11b) shows a manual interpretation of the fractures. In Figure 2.11c) the domain is discretised with triangles that matches all fractures and are all nearly equilateral. Figure 2.11d) shows flow simulations performed using the grid, where the fractures act as barriers.

At a pore-scale level the equations that describe transport are almost impossible to solve, because of the size of the reservoir and the limited computer capacity. Also, a pore-scale description of a reservoir is not available. Even though the pore-scale principles are important to understand the behaviour on the reservoir-scale, it is not beneficial to simulate with this accuracy. To simulate oil production knowledge about the state variables on a reservoir-scale is sufficient. With smaller cells the number of cells is higher, such that the choice of cell size is a trade-off between accuracy and computing time.

Geological models contain descriptions of porosity and permeability on a fine-scale grid, typically of the order of 10^7 cells. This number of grid cells is about a

factor 100 too large for today's computing power [26]. To bridge the gap between these two scales upscaling techniques [34, 43, 70, 98, 96, 97] are used to obtain suitable values for porosity, permeability and other property data for use in the coarse grid simulation.

2.2.6 Flow functions

Interactions between fluids and rock are described by capillary pressure and relative permeability functions.

Relative permeability

The relative permeability describes how well a fluid flows in presence of other fluids relative to if it was the only fluid present in the pores. Flow of a phase in presence of another can be viewed as single phase flow through a reduced pore space, with the wetting phase along the pore walls and the non-wetting phase in the middle. This leads to a reduced transmissibility for both phases.

Relative permeability is defined as the ratio between the effective permeability $k_{e\alpha}$ for phase α and the absolute permeability K [89]

$$k_{r,\alpha} = \frac{k_{e\alpha}}{K}, \tag{2.34}$$

The effective permeability $k_{e\alpha}$ describes the permeablility for specific saturations, and the sum of the effective permeabilities do not exceed the absolute permeability. When Darcy's law is extended from single- to multi-phase flow, the absolute permeability is replaced by an effective permeability.

The relative permeability depends on the fluid properties and the flow mechanisms, while the absolute permeability depends on the rock properties. Using the product of the absolute permeability and the relative permeability instead of the effective permeability, these contributions are separated.

The relative permeability is dimensionless and attain values between 0 and 1. The sum of the relative permeabilities for all phases is always less than 1

$$\sum_{i}^{n} k_{r,i} \leq 1, \tag{2.35}$$

where n is the number of phases.

Drainage is the process where a non-wetting phase displaces a wetting phase, while imbibition is the process where the wetting phases displaces the non-wetting phase. Hysteresis effects result in different relative permeability curves for drainage and imbibition. During drainage oil starts flowing at the critical oil saturation S_{oc}. When the residual water saturation S_{wc} is reached, the water phase

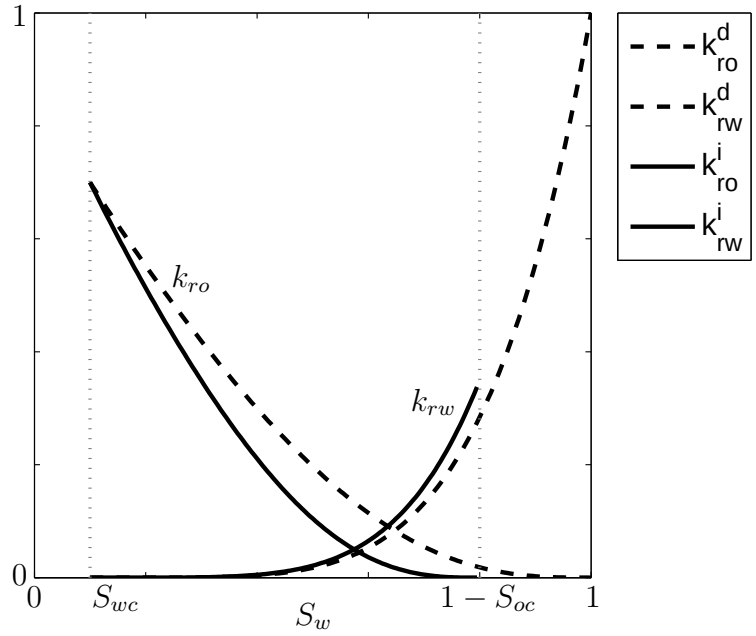

Figure 2.12: Relative permeability hysteresis for oil and water. The dashed curve is for primary drainage and the full curve is for imbibition.

is immobile and makes it impossible to inject more oil. Similarly, for imbibition the critical water saturation is the saturation for which water starts to flow, and the residual oil saturation is the saturation for which oil ceases to flow.

Figure 2.12 shows typical relperm curves for two-phase primary drainage and imbibition. Oil is injected into a completely water-filled medium until the residual water saturation is reached. When water is injected different relative permeability curves are followed, because of hysteresis effects. Trapping of oil makes the oil phase immobile before the start saturation for primary drainage is reached. The hysteresis effect is usually largest for the non-wetting phase, where the imbibition curve is significantly lower than the drainage curve [10]. If a process is reversed before the residual saturation is reached, different relative permeability curves are followed [52, 83].

In three-phase flow the relative permeability is a function of two saturations. The residual saturations, where the relative permeability reaches zero, can be visualised in a ternary diagram, shown in Figure 2.13. In the triangle in the middle all three fluids flow simultaneously. Along the sides of the ternary diagram one phase is immobile, while only one phase is mobile in the regions close to the corners.

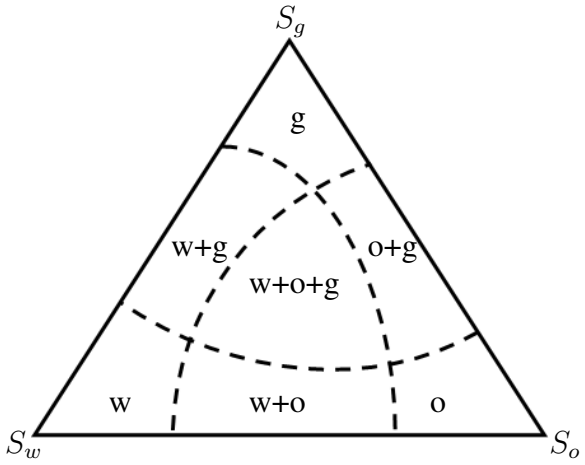

Figure 2.13: Ternary diagram illustrating which phases are mobile for different saturations, denoted by w for water, o for oil and g for gas. In the middle all phases are mobile, close to the edges one phase is immobile, and close to the corners only one phase is mobile.

Capillary pressure

When several immiscible phases coexist in pores in the reservoir there will be a discontinuity in pressure across the interface between the fluids. The capillary pressure is defined as the pressure difference between the non-wetting and wetting phases [89]

$$P_c = p_n - p_w, \tag{2.36}$$

where p_n and p_w are the pressures in the non-wetting and wetting phases, respectively. In a system with three phases, water, oil and gas, the capillary pressures between them are

$$\begin{aligned} P_{c,ow} &= p_o - p_w, \\ P_{c,go} &= p_g - p_o, \\ P_{c,gw} &= p_g - p_w. \end{aligned} \tag{2.37}$$

When two capillary pressures are given, the third can be found from the relation

$$P_{c,gw} = P_{c,ow} + P_{c,go}, \tag{2.38}$$

which can be verified by replacing the capillary pressures by the corresponding pressure differences between the phases.

During drainage the capillary pressure increases. As the saturation gets closer and closer to the residual saturation, the capillary pressure goes towards infinity.

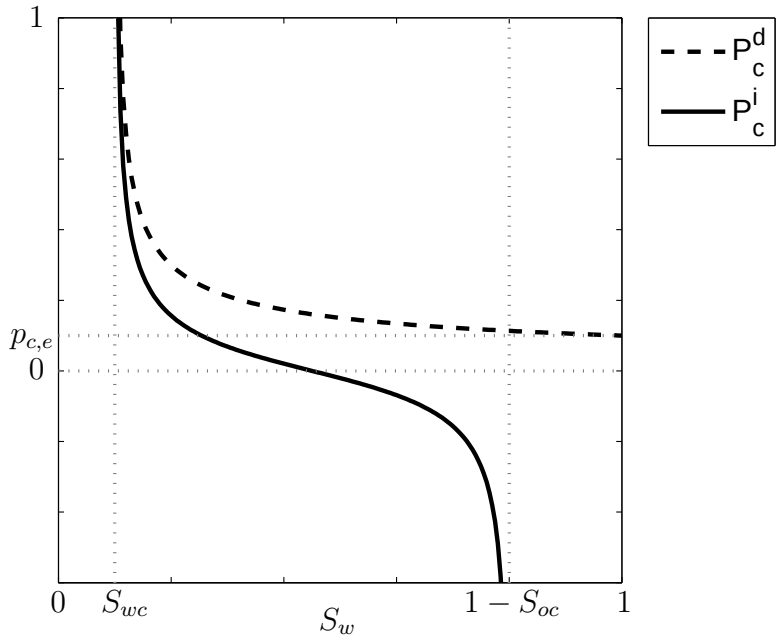

Figure 2.14: Capillary pressure hysteresis. The dashed curve is for primary drainage and the full curve is for imbibition.

During imbibition the capillary pressure decreases until in goes towards minus infinity at the residual saturation for the non-wetting phase.

From the Young-Laplace equation (Eq. (2.14)) it is obvious that a water-wet core has a positive capillary pressure function, while an oil-wet core has a negative capillary pressure function. A core with mixed wettability has a capillary pressure function with both positive and negative values.

Processes where the absolute value of the capillary pressure increases are forced and will not take place without an external force. On the contrary, processes where the absolute value of the capillary pressure decreases are spontaneous and will take place without an outer force. Thus, a water-wet core saturated with oil will imbibe water when it is in contact with water, and an oil-wet core saturated with water will imbibe oil in contact with oil.

Figure 2.14 shows a typical oil-water capillary pressure curve for primary drainage and imbibition. Initially, the wettability is water-wet and the system is completely water-filled, while after primary drainage the core has a mixed wettability. The difference between the oil and water pressures must be larger than the capillary entry pressure $p_{c,e}$ before oil starts to displace water during primary drainage. Water starts to displace oil from the larges pores, and as the capillary pressure increases smaller and smaller pores are reached. When the trapped water saturation is reached the capillary pressure curve goes towards infinity. For

the imbibition process to start the pressure difference between the oil and water phases must be smaller than the capillary pressure for the given saturation. When the capillary pressure reaches zero, water has to be forced into the system to flood the oil-wet pores. At the residual oil saturation no more water can be injected and the capillary pressure goes towards minus infinity.

The capillary pressure is inversely proportional to the radius of the pore (Eq. (2.14)) such that a pore with a small radius has a large capillary entry pressure, and vice versa. Therefore the shape of capillary pressure curve says something about the shape of the pore size distribution [79]. If the medium contains many pores of same size, their entry pressures are equal and they will be flooded simultaneously. A small change in pressure then leads to a large change in saturation. This will correspond to a horizontal capillary pressure curve. On the other hand, if all pore radii are equally represented in the medium, a small change in pressure will lead to a small change in saturations. The capillary pressure curve will now be linear.

Relative permeability and capillary pressure correlations

In practice empirical correlations for relative permeability and capillary pressure are often used. Typically, the correlations are functions of saturation, defined for the saturations where the fluids are mobile, defined by the residual saturations. The functions may also include parameters which are adjusted to the media, for example describing the pore distribution or the connectivity of the pores. By varying the parameters it is possible to obtain hysteresis effects, with different curves for drainage and imbibition.

Several empirical models that can be used to estimate relative permeability and capillary pressure exits [47]. From the Brooks-Corey model [16, 17, 28] the relative permeability for water is given as

$$k_{rw} = S_{we}^{\frac{2+3\lambda}{\lambda}}, \tag{2.39}$$

and the relative permeability for oil is given as

$$k_{rn} = (1 - S_{we})^2(1 - S_{we}\frac{2+\lambda}{\lambda}), \tag{2.40}$$

where λ is an empirical constant describing the pore size distribution. The effective water saturation is defined as

$$S_{we} = \frac{S_w - S_{wc}}{1 - S_{wc} - S_{nc}}, \tag{2.41}$$

where S_{wc} and S_{nc} is the residual saturation for the wetting and non-wetting phases, respectively. Similarly, the capillary pressure is given as

$$P_c(S_w) = p_{c,e}S_{we}^{-\frac{1}{\lambda}} \qquad \text{for } P_c \geq p_{c,e}, \tag{2.42}$$

where $p_{c,e}$ is the capillary entry pressure. To account for hysteresis the constants $p_{c,e}$ and λ can be different for imbibition and drainage. By combining a Brooks-Corey expression from a water-wet and an oil-wet reservoir, a relation for mixed-wet reservoirs [53, 45, 83] is given by

$$P_c = \frac{c_w}{S_{we}^{a_w}} + \frac{c_o}{S_{oe}^{a_o}}, \tag{2.43}$$

where

$$S_{oe} = \frac{1 - S_w - S_{oc}}{1 - S_{oc}} \tag{2.44}$$

is the effective oil saturation. The residual saturations S_{wc} and S_{oc} depend on the history of the reservoir. The constants a_w, a_o, c_w and c_o and are different for imbibition and drainage. c_o will be a negative constant and the three others will be positive.

The van Genuchten model [93, 67] expresses the relative permeabilities as

$$k_{rw} = S_{we}^{\epsilon}(1 - (1 - S_{we}^{\frac{1}{m}})^m)^2, \tag{2.45}$$

and

$$k_{rn} = (1 - S_{we})^{\gamma}(1 - S_{we}^{\frac{1}{m}})^{2m}, \tag{2.46}$$

where ϵ and γ describe the connectivity of the pores and m and n are parameters, usually satisfying the relation $m = 1 - \frac{1}{n}$. The corresponding capillary pressure is given as

$$P_c(S_w) = \frac{1}{\alpha}(S_{we}^{\frac{-1}{m}} - 1) \qquad \text{for } P_c > 0. \tag{2.47}$$

In three-phase flow it is often assumed that the oil-water capillary pressure is a function of water saturation, $P_{c,ow}(S_w)$, and gas-oil capillary pressure is a function of gas saturation, $P_{c,go}(S_g)$. Since the capillary pressure between gas and water is the sum of these two, this capillary pressure will depend on both water and gas saturations, $P_{c,gw}(S_w, S_g)$. Similarly, it is assumed that water relative permeability is a function of water saturation, $k_{rw}(S_w)$, and gas relative permeability is a function of gas saturation, $k_{rg}(S_g)$, while the oil relative permeability is a function of water and gas saturations, $k_{ro}(S_w, S_g)$ [28, 86].

Three-phase relative permeabilities are in practice found from two two-phase systems, one with the intermediate and the wetting phases and one with the intermediate and non-wetting phases [26]. In a system with a wetting, intermediate wetting and non-wetting phase, both the intermediate and non-wetting phases will be non-wetting to the wetting phase. Since they will act like a single non-wetting

phase, a system with only two phases is a good approximation. Similarly, the intermediate and wetting phases act as a wetting phase compared to the non-wetting phase. Thus water relative permeability is found from a water-oil system and oil relative permeability is found from a gas-oil system.

There are several ways to estimate the oil relative permeability [11], and the simplest is to use the product of water and gas permeabilities

$$k_{ro} = k_{row} k_{rog}, \tag{2.48}$$

where k_{row} is the oil relative permeability in a water-oil system and k_{rog} is the oil relative permeability in a gas-oil system.

Stone I [86] can also be used to estimate three-phase oil relative permeability by making the same assumption about saturation dependencies. The relative permeability for oil is estimated from interpolation between the oil relative permeabilities in a system with gas, oil and residual water and a system with water and oil. With a modified Stone I the relative permeability for oil will limit to the two-phase data. The relative permeability for oil is given as

$$k_{ro} = k_{rc} S_o^* \beta_w \beta_g, \tag{2.49}$$

where

$$\begin{aligned} \beta_w &= \frac{k_{row}(S_w)}{(1 - S_w^*)k_{rc}}, \\ \beta_g &= \frac{k_{rog}(S_g)}{(1 - S_g^*)k_{rc}}. \end{aligned} \tag{2.50}$$

The normalised saturations are

$$\begin{aligned} S_w^* &= \frac{S_w - S_{wc}}{1 - S_{wc} - S_{or}}, && S_{wc} \leq S_w \leq 1 - S_{or}, \\ S_o^* &= \frac{S_o - S_{or}}{1 - S_{wc} - S_{or}}, && S_{or} \leq S_o \leq 1 - S_{wc}, \\ S_g^* &= \frac{S_g}{1 - S_{wc} - S_{or}}, && 0 \leq S_g \leq 1 - S_{wc} - S_{or}, \end{aligned} \tag{2.51}$$

and the effective permeability of oil in presence of connate water is

$$k_{rc} = k_{row}(S_{wc}) = k_{rog}(S_g = 0). \tag{2.52}$$

S_{or} is the minimum oil saturation after injection of gas and water.

Stone II [87] formulates the relative permeability for oil as

$$k_{ro} = k_{rc}\left(\frac{k_{row}}{k_{rc}} + k_{rw}\right)\left(\frac{k_{rog}}{k_{rc}} + k_{rg}\right) - (k_{rw} + k_{rg}), \tag{2.53}$$

where k_{rg} is the relative permeability for gas in a system with oil and gas, and k_{rw} is the relative permeability for water in a system with oil and water.

In other models the three-phase oil relative permeability is found by linear interpolation between two-phase relative permeabilities k_{row} and k_{rog} or saturation weighted interpolation [8]. Different models are evaluated using several data sets [8, 33, 41], concluding that Stone I with normalised saturations often gives the best match.

Land [54, 55] related the maximum and residual saturation of the non-wetting phase to a constant C, which was used in an equation for calculating the mobile fraction of non-wetting phase during imbibition. These two equations are used in other hysteresis models, such as Killough's model [52] and Carlson's model [19].

The capillary pressure does not only depend on phase saturations, but also on interfacial tension, contact angle, permeability and porosity [89]. The Leverett J-function [59] approximates this relationship, such that the capillary pressure function for different fluids or different media can be estimated without performing new experiments. It accounts for changes in permeability, porosity and wettability of the reservoir as long as the general pore geometry is the same. The relation is given by

$$J(S_w) = \frac{P_c}{\sigma \cos\theta}\sqrt{\frac{K}{\phi}}. \tag{2.54}$$

In practice, this generalisation is not satisfactorily [20].

Chapter 3

Pore-Scale Models

To get better knowledge about flow functions, pore-scale models are useful tools. Flow functions estimated from a pore-scale model should reflect the pore-scale processes at the reservoir-scale in a good way, because they are based on the underlying pore-scale physics.

3.1 A capillary bundle model

A simplified porous media can be represented as a bundle of capillary tubes. The model described here has parallel cylindrical tubes different radius, volume, conductivity and wettability. In this model phase saturations can not be trapped and residual saturations are zero. Also more complex models with polygonal cross sections [46, 49] could be used, allowing mixed wettability within a single pore and oil drainage through layers in the crevices. Figure 3.1 shows a capillary bundle model filled with three different phases.

The phase occupancies are given by the phase pressures relative to the capillary entry conditions given by the Young Laplace equation (Eq. (2.14)). For each combination of capillary pressures unique saturations and relative permeabilities correspond. Varying the properties of the tubes results in different flow functions. The model provides us with a better understanding of pore occupancies and saturation dependencies.

Each tube contains only one phase and each side of the bundle is connected to vessels. We assume that the outlets contain the same phase as the tubes they are connected to and that the pressure in this phase is constant. The inlets contain the invading phase, and here the pressure is increasing gradually. This allows subsequent invasion of the pores in a piston-like manner. Each invasion of a tube is a two-phase displacement, but when taking the whole bundle into consideration, the displacements constitute a three-phase flow process.

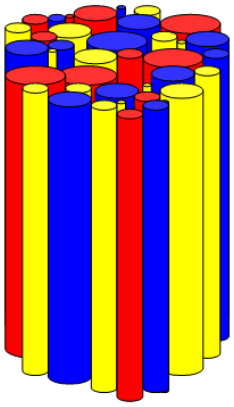

Figure 3.1: A capillary bundle model consisting of pores with different radii.

To find capillary pressures and relative permeabilities for given saturations the model is inverted iteratively. The flow functions from the capillary bundle model are consistent as they depend on the same underlying pore-physics.

3.1.1 A probabilistic model

In a realistic medium the wettability can not be described with a constant value for contact angles. Also pores with the same radius may have different wettability, resulting in that pores with same radius are not necessarily occupied by the same phase. The model that is used is described by van Dijke and Sorbie [90]. In this model the contact angles are distributed between a lower and an upper value, which can be different for different radii. Instead of one single value for contact angles, they are represented by a contact angle density function $\Psi_c(r, x)$, where $x = \cos\theta_{ow}$. The contact angle density function is normalised, such that

$$\int_{-1}^{1} \Psi_c(r, x)dx = 1. \tag{3.1}$$

The capillary entry pressure in the Young-Laplace equation (Eq. (2.14)) depends on the contact angle, such that when contact angles are distributed, the pairs of inequalities for occupancy of each phase (Eqs. (2.19), (2.18) and (2.17)) are replaced by joint probabilities. The probability $\pi_i(r)$ that a pore with radius r is

occupied by the phase i is given by

$$\begin{aligned}\pi_w(r) &= \text{Prob}[P_{gw} < P_{c,gw} \wedge P_{ow} < P_{c,ow}],\\ \pi_o(r) &= \text{Prob}[P_{go} < P_{c,go} \wedge P_{ow} > P_{c,ow}],\\ \pi_g(r) &= \text{Prob}[P_{gw} > P_{c,gw} \wedge P_{go} > P_{c,go}],\end{aligned} \tag{3.2}$$

which is the same as the number fraction of pores with a radius r that is occupied by phases water, oil and gas, respectively. Thus, the occupancy for water π_w is the probability that the pressure difference between the gas and water phases P_{gw} is smaller than the capillary entry pressure for gas and water $P_{c,gw}$ and the pressure difference between the oil and water phases P_{ow} is smaller than the capillary entry pressure for oil and water $P_{c,ow}$.

Since $\cos\theta_{gw}$ and $\cos\theta_{go}$ are linked linearly to $\cos\theta_{ow}$ (Eq. (2.8)), the gas-water and gas-oil contact angles can be expressed in terms of the oil-water contact angles. Thus, each inequality can be replaced by an inequality including the contact angle θ_{ow} and a separating line h_{ij} as

$$\begin{aligned}P_{go} > P_{c,go}: &\qquad \cos\theta_{ow} > h_{go}(r),\\ P_{gw} > P_{c,gw}: &\qquad \cos\theta_{ow} < h_{gw}(r),\\ P_{ow} > P_{c,ow}: &\qquad \cos\theta_{ow} < h_{ow}(r),\end{aligned} \tag{3.3}$$

where

$$\begin{aligned}h_{go}(r) &= \frac{P_{go}r - C'_{s,o} - 2\sigma_{go}}{C'_{s,o}},\\ h_{gw}(r) &= \frac{P_{gw}r - C'_{s,o} - 2\sigma_{go}}{C'_{s,o} + 2\sigma_{ow}},\\ h_{ow}(r) &= \frac{P_{ow}r}{2\sigma_{ow}}.\end{aligned} \tag{3.4}$$

$C'_{s,o}$ is given by

$$C'_{s,o} = \min(0, C_{s,o}), \tag{3.5}$$

where $C_{s,o}$ is the spreading coefficient for oil (Eq. (2.3)). The lines h_{ij} are called phase separating lines, because they separate the different phases in the $(r, \cos\theta_{ow})$-plane. Along a separating line h_{ij} the pressure difference P_{ij} between phases i and j is constant. The separating line h_{ij} intersects the $\cos\theta_{ow}$-axis in the point c_{ij}, given by

$$\begin{aligned}c_{go} &= \frac{-C'_{s,o} - 2\sigma_{go}}{C'_{s,o}},\\ c_{gw} &= \frac{-C'_{s,o} - 2\sigma_{go}}{C'_{s,o} + 2\sigma_{ow}},\\ c_{ow} &= 0.\end{aligned} \tag{3.6}$$

As a consequence of the Bartell-Osterhof equation (Eq. (2.7)) the three separating lines intersect in a point $(\overline{r}, \overline{c})$. The coordinates for the intersection point are

$$\begin{aligned} \overline{r} &= \frac{-2\sigma_{ow}(C'_{s,o} + 2\sigma_{go})}{C'_{s,o}P_{ow} - 2\sigma_{ow}P_{go}}, \\ \overline{c} &= \frac{-P_{ow}(C'_{s,o} + 2\sigma_{go})}{C'_{s,o}P_{ow} - 2\sigma_{ow}P_{go}}. \end{aligned} \tag{3.7}$$

Knowing the intersection point $(\overline{r}, \overline{c})$ is equivalent to knowing the pressure differences between the phases.

By using Eq. (3.3) the two-phase occupancies can be expressed as

$$\begin{aligned} \pi_g^{go}(r) &= \text{Prob}[\cos\theta_{ow} > h_{go}(r; P_{go})], \\ \pi_g^{gw}(r) &= \text{Prob}[\cos\theta_{ow} < h_{gw}(r; P_{gw})], \\ \pi_o^{ow}(r) &= \text{Prob}[\cos\theta_{ow} < h_{ow}(r; P_{ow})], \end{aligned} \tag{3.8}$$

where π_k^{ij} is the occupancy of the phase k in a two-phase system with phases i and j. In a two-phase system with phases i and j the occupancies will sum up to one, such that

$$\pi_i^{ij} + \pi_j^{ij} = 1. \tag{3.9}$$

From this equation the two-phase occupancies π_o^{go}, π_w^{gw} and π_w^{ow} can be found.

The two-phase occupancies are calculated by integration over the contact angle density function $\Psi_c(r, x)$ with respect to the random variable $x = \cos\theta_{ow}$, such that

$$\text{Prob}[\cos\theta_{ow} < h_{ij}(r)] = \int_{-\infty}^{h_{ij}(r)} \Psi_c(r, x)dx, \tag{3.10}$$

or

$$\text{Prob}[\cos\theta_{ow} > h_{ij}(r)] = \int_{h_{ij}(r)}^{\infty} \Psi_c(r, x)dx, \tag{3.11}$$

for a given h_{ij}.

The three-phase occupancies are found as joint probabilities in terms of two-phase occupancies

$$\pi_w(r) = \begin{cases} \pi_w^{ow}(r) & = \int_{h_{ow}(r)}^{1} \Psi_c(r, x)dx, \quad \text{for } r < \overline{r}, \\ \pi_w^{gw}(r) & = \int_{h_{gw}(r)}^{1} \Psi_c(r, x)dx, \quad \text{for } r > \overline{r}, \end{cases} \tag{3.12}$$

$$\pi_o(r) = \begin{cases} \pi_o^{ow}(r) & = \int_{-1}^{h_{ow}(r)} \Psi_c(r, x)dx, \quad \text{for } r < \overline{r}, \\ \pi_o^{go}(r) & = \int_{-1}^{h_{go}(r)} \Psi_c(r, x)dx, \quad \text{for } r > \overline{r}, \end{cases} \tag{3.13}$$

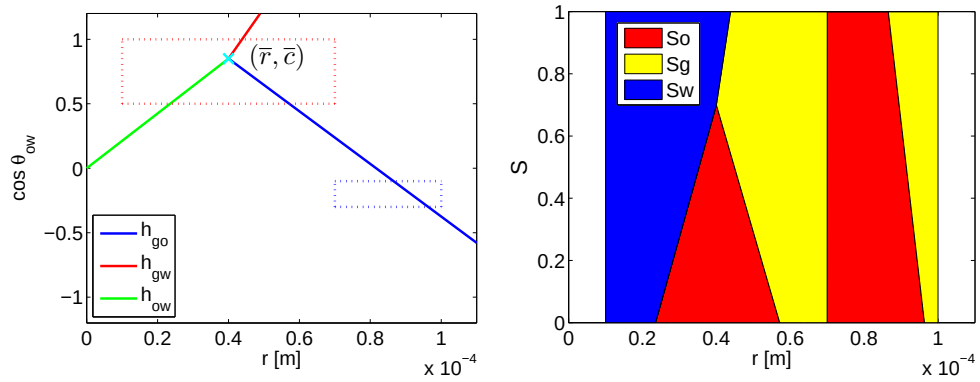

a) b)

Figure 3.2: a) The $(r, \cos\theta_{ow})$-plane for a mixed-wet system, where small pores are water-wet and large pores are oil-wet. For radii $0.1{\cdot}10^{-4} < r < 0.7{\cdot}10^{-4}$ m the wettability is given by $0.5 < \cos\theta_{ow} < 1$ and for radii $0.7 \cdot 10^{-4} < r < 1 \cdot 10^{-4}$ m the wettability is given by $-0.3 < \cos\theta_{ow} < -0.1$. The phases are separated by the lines h_{ij}, which intersect in a point $(\overline{r}, \overline{c})$, corresponding to a prescribed pressure combination. The contact angle density function Ψ_c is only non-zero inside the dashed regions. b) Corresponding phase occupancies for a uniform contact angle density function Ψ_c.

and

$$\pi_g(r) = \begin{cases} 0 & \text{for } r < \overline{r}, \\ \pi_g^{gw}(r) + \pi_g^{go}(r) - 1 \;\; = \int_{h_{go}(r)}^{h_{gw}(r)} \Psi_c(r,x)dx & \text{for } r > \overline{r}. \end{cases} \tag{3.14}$$

Figure 3.2 illustrates the model for a mixed-wet system. Figure 3.2a) shows the $(r, \cos\theta_{ow})$-plane, where the support of the contact angle density function Ψ_c is inside the dashed rectangles. The lines h_{ij} separate the phases in the plane, resulting in the phase occupancies in Figure 3.2b).

Based on the two-phase occupancies, the saturation S_j^{ij} and the relative permeability $k_{r,j}^{ij}$ for phase j in a two-phase system with phases i and j are found by

$$S_j^{ij} = \int_0^\infty \pi_j^{ij}(r)\varphi_s(r)V(r)dr, \tag{3.15}$$

and

$$k_{r,j}^{ij} = \int_0^\infty \pi_j^{ij}(r)\varphi_s(r)g(r)dr, \tag{3.16}$$

respectively, where $\varphi_s(r)$ is the density function for pore sizes, $V(r)$ is the volume function and $g(r)$ is the conductance function.

The pore size density function determines the density of pores of different sizes. It is given by

$$\varphi_s(r) \propto r^n, \tag{3.17}$$

and is normalised, such that

$$\int_{r_{min}}^{r_{max}} \varphi_s(r)dr = 1. \tag{3.18}$$

We have used $n = 0$, which means that all radii are equally represented in the bundle.

The volume function determines the relation between the volume of pores with different radii. It is given by

$$V(r) \propto r^\nu, \tag{3.19}$$

and is normalised with respect to the total volume of the system, such that

$$\int_{r_{min}}^{r_{max}} V(r)dr = 1. \tag{3.20}$$

We have used $\nu = 2$, corresponding to cylindrical tubes.

The conductance function has the same role for relative permeability as the volume function has for saturation. It is given by

$$g(r) \propto r^\lambda, \tag{3.21}$$

and is normalised with respect to the total conductivity, such that

$$\int_{r_{min}}^{r_{max}} g(r)dr = 1. \tag{3.22}$$

A conductance exponent $\lambda = 4$ reflects conductance in cylindrical tubes, in accordance with Poiseuille's law [60].

The saturation S_j and relative permeability $k_{r,j}$ in a three-phase system are found from the three-phase occupancies by

$$S_j = \int_0^\infty \pi_j(r)\varphi_s(r)V(r)dr, \tag{3.23}$$

and

$$k_{r,j} = \int_0^\infty \pi_j(r)\varphi_s(r)g(r)dr. \tag{3.24}$$

The expressions satisfy

$$S_w + S_o + S_g = 1, \tag{3.25}$$

and

$$k_{r,w} + k_{r,o} + k_{r,g} = 1. \tag{3.26}$$

Eq. (3.26) is a result from the fact that a capillary bundle is completely accessible and will not apply for a realistic porous medium. From this forward model we can find saturations and relative permeabilities in a capillary bundle of tubes for given capillary pressures.

3.1.2 Analysis of occupancies

The phase occupancies are uniquely determined from the intersection point $(\overline{r}, \overline{c})$. Therefore, the location of the intersection point relative to the support of the contact angle density function in the $(r, \cos\theta)$-plane provides us with information about the number of present phases and also the saturation-dependencies of the flow functions. Saturation-dependencies describe whether a three-phase relative permeability depends only on its own saturation and whether it can be linked to the corresponding two-phase relative permeability. This has been studied by van Dijke and Sorbie [90].

For distributed contact angles an intersection point located inside the support of the contact angle density function always correspond to three-phase occupancies, while an intersection point located outside or on the boundary of the support can correspond to various numbers of phases. For three-phase systems all occupancies π_w, π_o and π_g must be non-zero. Looking at the extreme positions of the separating lines, for which these still intersect with the support, it is possible to find the regions where the intersection point corresponds to three-phase occupancies.

This is illustrated in Figure 3.3 for a contact angle density function with connected support. The dashed rectangle shows the support and the lines are the extreme positions of the separating lines. If the intersection point is located inside the shaded triangles or inside the support, all occupancies π_w, π_o and π_g are non-zero and three phases are therefore present. For intersection points located outside this area occupancies will be either one- or two-phase. One- or two-phase occupancies are determined by only one separating line, since the last two separating lines do not intersect with the support and will therefore not effect the occupancies. Thus, different intersection points correspond to the same occupancies. To make a unique relation from the two-phase occupancies to an intersection point the two-phase region is defined to be on the boundary of the three-phase region.

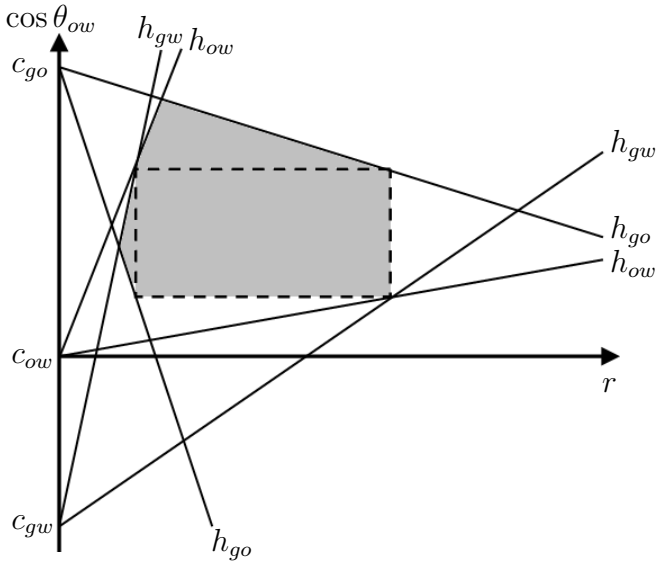

Figure 3.3: Illustration of the three-phase region. The support of contact angle distribution Ψ_c is bounded by the dashed rectangle, the extremes of the separating lines h_{ij} are shown as lines and the three-phase region is shown in grey.

The transition between two- and three-phase pressures will then be smooth and the occupancies will correspond to a unique intersection point. When the contact angle density function consists of disconnected regions the analysis of the $(r, \cos\theta_{ow})$-plane is more complicated [90].

When the intersection point is located within the support, all phases are bounded by two separating lines, such that all three-phase occupancies depend on two two-phase occupancies. This results in multiple saturation dependencies, which means that none of the three-phase relative permeabilities can be written as a combination of the corresponding two-phase relative permeabilities.

For three-phase occupancies where the intersection point is located outside the support, two of the phases are bounded by only one separating line, while the last phase is bounded by two separating lines. The relative permeabilities for the phases bounded by only one separating line will only depend on their own phase saturation. This behaviour is called simple saturation-dependency. The phase bounded by two separating lines is the intermediate-wetting phase.

Mixed-wet and fractionally-wet systems with contact angles which are not distributed will always show simple saturation-dependencies, since the support does not have an interior. This has been described by van Dijke et al. [92].

A relative permeability function showing simple saturation-dependency may equal the relative permeability for a two-phase system where phases are separated by the same separating line. In this case the occupancy for the given phase

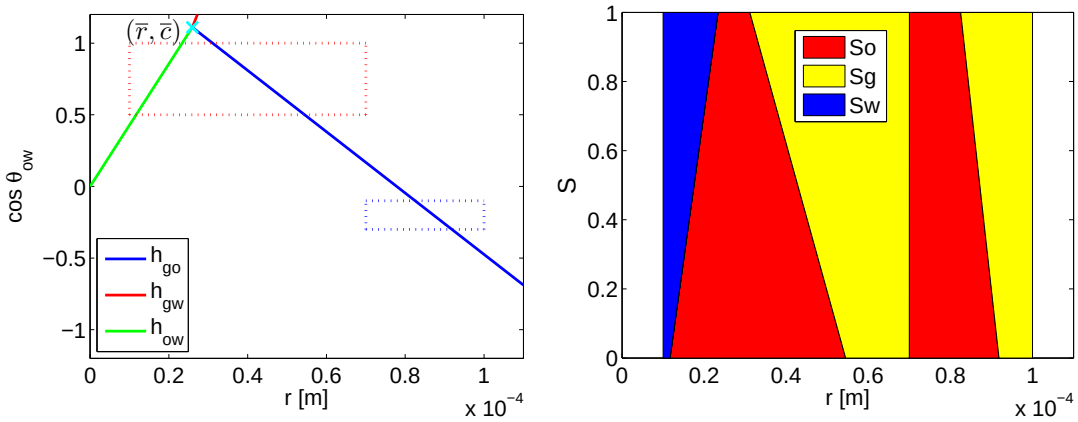

Figure 3.4: a) The $(r, \cos\theta_{ow})$-plane for a mixed-wet system where the intersection point is located outside the support of Ψ_c. Water and gas relative permeabilities depend only on their own saturations and are genuine. Oil is the intermediate wetting phase, such that oil relative permeability depends on two saturations. b) The corresponding phase occupancies π_j for a uniform contact angle density function Ψ_c.

equals the corresponding two-phase occupancy. Thus, the relative permeability for phase i is genuine if $k_{r,i}(S_i) = k^{ij}_{r,i}(S_i)$. If it is not possible to identify the three-phase relative permeability with its two-phase counterpart, the relative permeability is non-genuine. The expression for three-phase water relative permeability (Eq. (3.24)) can be written as a sum of two integrals in terms of two-phase occupancies by

$$k_{r,w} = \int_{r_{min}}^{\bar{r}} \pi_w^{ow}(r)\varphi_s(r)g(r)dr + \int_{\bar{r}}^{r_{max}} \pi_w^{gw}(r)\varphi_s(r)g(r)dr. \tag{3.27}$$

This expression can not in general be written in terms of two-phase relative permeabilities (Eq. (3.16)), since the limits of the integrals are different.

If the support of the contact angle density function is not well connected, one of the phases may not be bounded by any separating lines. Then it is possible to move the intersection point along the separating line between the other two phases without changing the occupancies, and therefore, a phase occupancy will not correspond to a unique intersection point. The relative permeability for the phase which is not bounded by a separating line is constant in a neighbourhood of the corresponding saturations.

In Figure 3.4 oil is the intermediate wetting phase. The oil relative permeability depends on two saturations, while the water and gas relative permeabilities

depend only on their own saturations and are equal to their two-phase counterparts, corresponding to genuine simple saturation-dependency.

3.1.3 Inversion of the capillary bundle model

The capillary bundle model provides us with relative permeabilities and saturations for given capillary pressures. To find the capillary pressure as a function of saturation, an inversion of the capillary bundle model is necessary. This is done by an iterative approach following van Dijke and Sorbie [90].

The phase saturations for given phase pressures are found from Eq. (3.23). Moving the intersection point corresponds to changing the phase pressures. This results in different phase saturations, unless the intersection point is located in an anomalous region. Outside anomalous regions a combination of three-phase saturations corresponds to a unique phase occupancy and a unique combination of phase pressures.

To get from the current saturations (S_w, S_o, S_g) to the target saturations (S_w^*, S_o^*, S_g^*) the intersection point is moved a distance $\Delta\overline{y}$ through the $(r, \cos\theta_{ow})$-plane along the line

$$\tilde{h} = \frac{\overline{c} - \tilde{c}}{\overline{r}} r + \tilde{c}, \tag{3.28}$$

which goes through the point $(\overline{r}, \overline{c})$ and intersects the $\cos\theta_{ow}$-axis in $\tilde{c}$.

Figure 3.5 shows the separating lines in the $(r, \cos\theta_{ow})$-plane for two different intersection points.

To derive equations for the change in saturation when the intersection point is moved in the direction $\overline{y}$, described by the line $\tilde{h}$, the expressions for phase occupancies π_i (Eqs. (3.12), (3.13) and (3.14)) are substituted into the expression for the saturation (Eq. (3.23)), giving

$$\begin{aligned}
S_w(\overline{r}, \overline{c}) &= \int_{r_{min}}^{r_{max}} \int_{h_{ow(r;\overline{r},\overline{c})}}^{\infty} \Psi_c(r,x) dx \varphi_s(r) V(r) dr \\
&\quad + \int_{\overline{r}}^{r_{max}} \int_{h_{gw(r;\overline{r},\overline{c})}}^{\infty} \Psi_c(r,x) dx \varphi_s(r) V(r) dr, \\
S_o(\overline{r}, \overline{c}) &= \int_{r_{min}}^{\overline{r}} \int_{-\infty}^{h_{ow(r;\overline{r},\overline{c})}} \Psi_c(r,x) dx \varphi_s(r) V(r) dr \\
&\quad + \int_{\overline{r}}^{r_{max}} \int_{-\infty}^{h_{go(r;\overline{r},\overline{c})}} \Psi_c(r,x) dx \varphi_s(r) V(r) dr, \\
S_g(\overline{r}, \overline{c}) &= \int_{\overline{r}}^{r_{max}} \int_{h_{go(r;\overline{r},\overline{c})}}^{h_{gw(r;\overline{r},\overline{c})}} \Psi_c(r,x) dx \varphi_s(r) V(r) dr.
\end{aligned} \tag{3.29}$$

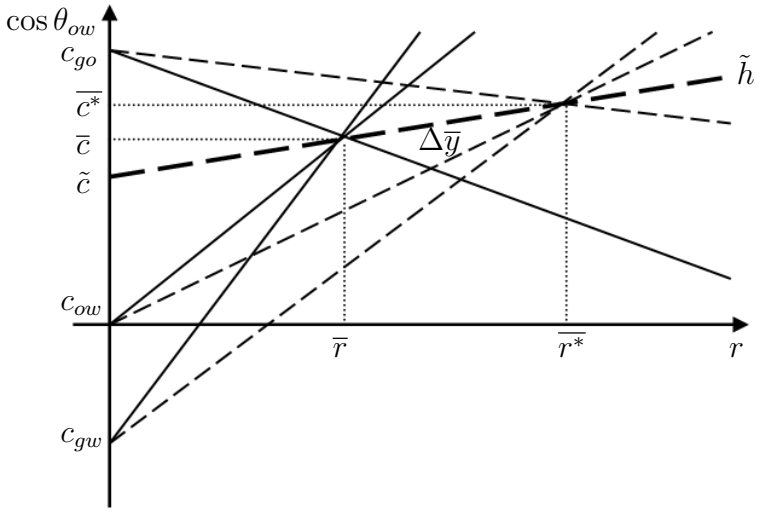

Figure 3.5: The separating lines h_{ij} for two different intersection points $(\overline{r}, \overline{c})$ in the $(r, \cos\theta_{ow})$-plane. The second intersection point is found by moving a distance $\Delta\overline{y}$ along the line $\tilde{h}$.

Here separating lines are expressed in terms of the intersection point instead of the phase pressures (Eq. (3.4)), such that

$$h_{ij}(r; \overline{r}, \overline{c}) = \frac{\overline{c} - c_{ij}}{\overline{r}} r + c_{ij}, \tag{3.30}$$

where c_{ij} is the intersection between the separating line h_{ij} and the $\cos\theta_{ow}$-axis. Using the Fundamental Theorem of Calculus [2]

$$\frac{d}{dx} \int_a^{g(x)} f(t)dt = f(g(x)) \frac{dg(x)}{dx}, \tag{3.31}$$

the differentiation of S_w with respect to $\overline{r}$ is

$$\begin{aligned} \frac{\partial S_w}{\partial \overline{r}} = & \int_{h_{ow}(\overline{r};\overline{r},\overline{c})}^{h_{gw}(\overline{r};\overline{r},\overline{c})} \Psi_c(\overline{r}, x)dx\varphi_s(\overline{r})V(\overline{r}) \\ & - \int_{\overline{r}}^{r_{max}} \Psi_c(r, h_{ow}(r; \overline{r}, \overline{c})) \frac{\partial h_{ow}}{\partial \overline{r}}(r; \overline{r}, \overline{c})\varphi_s(r)V(r)dr \\ & - \int_{r_{min}}^{\overline{r}} \Psi_c(r, h_{gw}(r; \overline{r}, \overline{c})) \frac{\partial h_{gw}}{\partial \overline{r}}(r; \overline{r}, \overline{c})\varphi_s(r)V(r)dr. \end{aligned} \tag{3.32}$$

Similarly, differentiation of S_w with respect to $\overline{c}$ is

$$\begin{aligned}\frac{\partial S_w}{\partial \overline{c}} = &\int_{h_{ow}(\overline{r};\overline{r},\overline{c})}^{h_{gw}(\overline{r};\overline{r},\overline{c})} \Psi_c(\overline{r},x)dx\varphi_s(\overline{r})V(\overline{r}) \\ &- \int_{\overline{r}}^{r_{max}} \Psi_c(r,h_{ow}(r;\overline{r},\overline{c}))\frac{\partial h_{ow}}{\partial \overline{c}}(r;\overline{r},\overline{c})\varphi_s(r)V(r)dr \\ &- \int_{r_{min}}^{\overline{r}} \Psi_c(r,h_{gw}(r;\overline{r},\overline{c}))\frac{\partial h_{gw}}{\partial \overline{c}}(r;\overline{r},\overline{c})\varphi_s(r)V(r)dr.\end{aligned} \tag{3.33}$$

The first integral in each equation equals zero, because the lower and upper limits for integration are equal

$$h_{gw}(\overline{r};\overline{r},\overline{c}) = h_{ow}(\overline{r};\overline{r},\overline{c}) = \overline{c}. \tag{3.34}$$

Differentiation with respect to the direction $\overline{y}$ along $\tilde{h}$ is

$$\frac{d}{d\overline{y}} = \frac{\partial}{\partial \overline{r}} + \frac{\partial \tilde{h}}{\partial r}\frac{\partial}{\partial \overline{c}}, \tag{3.35}$$

such that differentiation of h_{ij} in the direction of $\overline{y}$ is

$$\frac{dh_{ij}}{d\overline{y}} = \frac{\partial h_{ij}}{\partial \overline{r}} + \frac{\partial \tilde{h}}{\partial r}\frac{\partial h_{ij}}{\partial \overline{c}}. \tag{3.36}$$

By writing out the derivatives this simplifies to

$$\frac{dh_{ij}}{d\overline{y}} = \frac{c_{ij} - \tilde{c}}{\overline{r}^2}r. \tag{3.37}$$

Similarly, the differentiation of S_w in the direction of $\overline{y}$ is

$$\frac{dS_w}{d\overline{y}} = \frac{\partial S_w}{\partial \overline{r}} + \frac{\partial \tilde{h}}{\partial r}\frac{\partial S_w}{\partial \overline{c}}. \tag{3.38}$$

By writing out all terms and then using Eq. (3.37) this equation can be written as

$$\frac{dS_w}{d\overline{y}} = -(c_{ow} - \tilde{c})I_{ow} - (c_{gw} - \tilde{c})I_{gw}. \tag{3.39}$$

By the same approach we get

$$\frac{dS_o}{d\overline{y}} = (c_{ow} - \tilde{c})I_{ow} + (c_{go} - \tilde{c})I_{go} \tag{3.40}$$

and

$$\frac{dS_g}{d\overline{y}} = (c_{gw} - \tilde{c})I_{gw} - (c_{go} - \tilde{c})I_{go}. \tag{3.41}$$

The integrals I_{ij} are

$$\begin{aligned} I_{ow}(\overline{r},\overline{c}) &= \int_{r_{min}}^{\overline{r}} \Psi_c(r, h_{ow}(r;\overline{r},\overline{c}))\frac{r}{\overline{r}^2}\varphi_s(r)V(r)dr, \\ I_{go}(\overline{r},\overline{c}) &= \int_{\overline{r}}^{r_{max}} \Psi_c(r, h_{go}(r;\overline{r},\overline{c}))\frac{r}{\overline{r}^2}\varphi_s(r)V(r)dr, \\ I_{gw}(\overline{r},\overline{c}) &= \int_{\overline{r}}^{r_{max}} \Psi_c(r, h_{gw}(r;\overline{r},\overline{c}))\frac{r}{\overline{r}^2}\varphi_s(r)V(r)dr. \end{aligned} \tag{3.42}$$

This is valid when oil is non-spreading. Spreading oil is treated as a special case.

To solve the Eqs. (3.39), (3.40) and (3.41) iteratively the differentials $\frac{dS_i}{d\overline{y}}$ are replaced by the differences $\frac{\Delta S_i}{\Delta\overline{y}}$, where $\Delta S_i = S_i^* - S_i$. We have three equations and two unknowns, $\Delta\overline{y}$ and $\tilde{c}$, such that a solution is found by combining any two of the equations. Combining the Eqs. (3.39) and (3.40) gives

$$\tilde{c} = \frac{\Delta S_o(c_{ow}I_{ow} + c_{gw}I_{gw}) + \Delta S_w(c_{ow}I_{ow} + c_{go}I_{go})}{\Delta S_w(I_{ow} + I_{go}) + \Delta S_o(I_{ow} + I_{gw})} \tag{3.43}$$

and

$$\Delta\overline{y} = \frac{\Delta S_o}{(c_{ow} - \tilde{c})I_{ow} + (c_{go} - \tilde{c})I_{go}}. \tag{3.44}$$

By Pythagoras rule the step length satisfies

$$\Delta\overline{y}^2 = \Delta\overline{r}^2 + \Delta\overline{c}^2, \tag{3.45}$$

where $\Delta\overline{r}$ and $\Delta\overline{c}$ is related through the slope of $\tilde{h}$

$$\Delta\overline{c} = \Delta\overline{r}\frac{\overline{c} - \tilde{c}}{\overline{r}}. \tag{3.46}$$

Thus, the change in intersection point along the r- and $\cos\theta$- axes is

$$\begin{aligned} \Delta\overline{r} &= \frac{\Delta\overline{y}}{\sqrt{1 + (\overline{c} - \frac{\tilde{c}}{\overline{r}})^2}}, \\ \Delta\overline{c} &= \frac{\Delta\overline{y}}{\sqrt{1 + (\overline{c} - \frac{\tilde{c}}{\overline{r}})^2}}\frac{\overline{c} - \tilde{c}}{\overline{r}}. \end{aligned} \tag{3.47}$$

The updated intersection point is

$$\begin{aligned} \overline{r}^{k+1} &= \overline{r}^k + \Delta\overline{r}^k, \\ \overline{c}^{k+1} &= \overline{c}^k + \Delta\overline{c}^k, \end{aligned} \tag{3.48}$$

where the superscript k is the iteration index.

Special cases

For some special cases alternative equations are used in all or some of the iterations.

For spreading oil the spreading coefficient $C_{s,o}$ is 0, resulting in a vertical separating line between gas and oil. By a similar approach as for the spreading case we derive the equations

$$\begin{aligned}
\frac{dS_w}{d\overline{y}} &= -(c_{ow} - \tilde{c})I_{ow} - (c_{gw} - \tilde{c})I_{gw}, \\
\frac{dS_o}{d\overline{y}} &= (c_{ow} - \tilde{c})I_{ow} + I'_{go}, \\
\frac{dS_g}{d\overline{y}} &= (c_{gw} - \tilde{c})I_{gw} - I'_{go},
\end{aligned} \tag{3.49}$$

where

$$I'_{go}(\overline{r}, \overline{c}) = \int_{\infty}^{\overline{c}} \Psi_c(\overline{r}, h_{gw}(r; \overline{r}, \overline{c}))dx\varphi_s(r)V(r). \tag{3.50}$$

Vertical movement of the intersection point can not be described by the line $\tilde{h}$ and therefore other equations are obtained. The differential for vertical movement is

$$\frac{d}{d\overline{y}} = \frac{\delta}{\delta\overline{c}}. \tag{3.51}$$

By using this differential, Eqs. (3.49) are modified to

$$\begin{aligned}
\frac{\partial S_w}{\partial\overline{y}} &= -\overline{r}I_{ow} - \overline{r}I_{gw}, \\
\frac{\partial S_o}{\partial\overline{y}} &= \overline{r}I_{ow} + \overline{r}I_{go}, \\
\frac{\partial S_g}{\partial\overline{y}} &= \overline{r}I_{gw} - \overline{r}I_{go}.
\end{aligned} \tag{3.52}$$

These equations only have one unknown, and the step length is found by solving one of the equations for $\Delta\overline{y}$.

Another special case is when the denominator for $\tilde{c}$ in Eq. (3.43) equals zero. Then alternative expressions can be derived by combining expressions for two other phases, either Eqs. (3.39) and (3.41) or Eqs. (3.40) and (3.41). If all expressions for $\tilde{c}$ have a zero denominator, the intersection point corresponds to two-phase occupancy. This will be taken into consideration when calculating the step length $\Delta\overline{y}$.

The intersection points corresponding to two-phase occupancies are defined to be on the boundary of the three-phase region to provide uniqueness between the capillary pressures and the phase saturations. Thus, if the intersection point is located outside the three-phase region, the previous step length is divided by two until it is inside or on the boundary of the three-phase region.

Also when the intersection point is located in a three-phase region, the calculation of the step size is not straight forward. The denominator of $\Delta\overline{y}$ in Eq. (3.44) may equal zero, leading to an infinite step size. To obtain an alternative expression for $\Delta\overline{y}$, the expression for $\tilde{c}$ in Eq. (3.44) is substituted into either Eq. (3.40) or Eq. (3.41). The denominator may equal zero when the intersection point moves along one of the separating lines, such that $\tilde{c} = c_{ij}$. When the movement is along the separating line between phase i and j, the sign of the step size is found from the remaining phase and the absolute value of the step size is set to a constant value, which is reduced if the intersection point oscillate between two points.

Scaling

The axes in the $(r, \cos\theta_{ow})$-plane are of different orders of magnitude and this leads to numerical problems due to a finite number of decimals in the computations. Therefore, the radii are mapped to values between 0 and R_{max} by the transformation

$$R = \frac{R_{max}}{r_{max}} r. \tag{3.53}$$

The line giving the direction of movement of the intersection point is now given by

$$\tilde{H} = \frac{\overline{c} - \tilde{c}}{\overline{R}} R + \tilde{c}, \tag{3.54}$$

where $\overline{R}$ is the scaled value of $\overline{r}$. Differentiation with respect to the direction $\tilde{H}$ leads to modifications in Eqs. (3.39), (3.40) and (3.41).

3.2 Network models

In a realistic porous medium the pores are interconnected. Therefore, the major weakness of the bundle of tubes model lies in the absence of cross-connections between the tubes. This motivates the development of models where the capillary tubes are connected in two- or three-dimensional networks [12, 23, 42, 75, 76, 91]. The network models are used to provide improved understanding of multiphase systems.

In contrast to the capillary bundle model described in Section 3.1, phases can be trapped in a network model, leading to residual saturations. In addition, important features such as wetting and spreading layers and wettability alteration are implemented, such that the relative permeability and capillary pressure functions are history-dependent. The accuracy of a network model can be found by comparing displacement patterns and flow functions with results from micro model experiments.

3.2.1 Background

Complex network models have evolved over time from simpler models, such as the capillary bundle model [77], which was frequently used to analyse flow functions from mercury experiments. Another early approach is the conduit models [21, 22], which consists of a single flow channel with a specified radius. The interconnectedness in conduit models is implicitly included through a parameter for tortuosity.

Fatt [40] brought the models one step further by introducing a two-dimensional interconnected network of pores. He made the assumption that fluid invasion depends on capillary pressure only and that there is capillary equilibrium in the network. In addition, he used an analogue between electrical current and fluid flow, instead of the hydrodynamic laws. A conclusion from this work is that both the capillary pressure and the relative permeability are sensitive to the structure of the network.

The percolation theory describes the behaviour of connected clusters in mathematical networks. This is associated with the work of Broadbent and Hammersley [15] and has been important in the development of network models. The theory is based on the static properties of the medium and does not take the fluid transport process into account [58]. Heiba et al. [44] used the percolation theory to calculate two-phase relative permeabilities. Motivated by the study of two-phase flow in porous media Wilkinson and Willemsen [99] developed the invasion percolation theory, which also takes the fluid transport process into account by mapping the entry pressure for each pore to an occupancy probability. Invasion percolation processes are frequently used to describe fluid flow in network models [12, 14].

A porous medium consists of void spaces which are connected by thin pathways. It is therefore natural to build network models that distinguish between pores and throats [13, 14, 42]. Most of the void space is located in the pores, such that some models neglect the volume of the throats in volume calculations [14].

3.2.2 The Heriot Watt network model

The Heriot Watt network model [91] was built to develop better understanding of three-phase flow processes in porous media of heterogeneous wettability. A visualisation of the network is shown in Figure 3.6. It is three-dimensional and can handle immiscible incompressible flow. The network model is described by three types of input parameters: Pore properties, fluid properties and wettability properties.

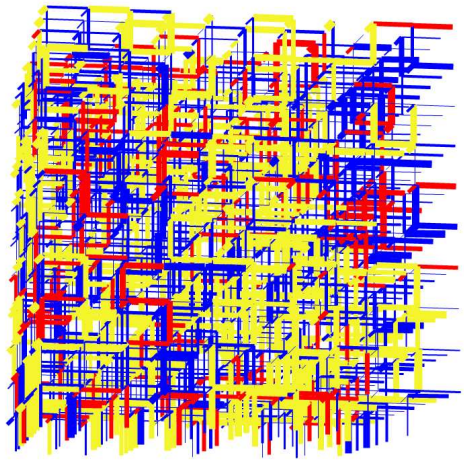

Figure 3.6: A three-dimensional network of pores from the Heriot Watt network model.

The pore properties describe the geometry of the network. The network is cubic and consists of pores following x-, y- and z-directions. Every pore has a radius and a volume and is connected to other pores. The pore size, volume and conductivity distributions are the same functions as for the capillary bundle model. In addition a coordination number is introduced. The coordination number describes the connectivity, given by the average number of pores that meet at the nodes where the pores are connected. If the coordination number is six, the network is fully connected. For coordination numbers less than six, random pores are removed until the network has the given average coordination number. By using a random seed it is possible to create the same network over again.

The fluid properties are interfacial tensions between the fluids and densities

for each phase. If gravity is neglected, the densities are not used.

As for the capillary bundle model, the wettability is given by the contact angle between oil and water and is distributed between lower and upper bounds for different radii. To make the wettability state closer to a realistic reservoir an ageing option is included. Thus, after primary drainage the wettability is altered based on the phase occupying each pore, such that the water-filled and oil-filled pores have different wettability distributions. In addition, threshold values for occurrence of films along the pore walls are defined. A phase which is not connected to the outlet of the network can escape through films or spreading layers along the pore walls. In the network model this is included by specifying minimum or maximum contact angles for films of one phase to form around another phase.

In the capillary bundle model all pores are accessible, such that a displacement takes place if the conditions for phase pressures relative the capillary entry pressures correspond to a displacement. This is different for a network model, where pores with different entry conditions are connected to each other. When a phase is injected into the network, not all pores are accessible, and this makes the displacement criteria more complicated. This is explained with an example where oil is injected into a network with oil and water. If the capillary pressure is large enough for oil to invade a pore there are two reasons that can prevent it from happening [85]:

1. If there are no neighbouring pores filled with oil, the oil phase is not able to see the specific pore. A pore is only accessible if there is a continuous path of oil-filled pores from the inlet.

2. The water in the pore must be able to flow out of the pore to make space for the oil. If this is not possible we say that the water is trapped in the pore. Trapping happens if

   (a) there are no continuous paths of water-filled pores from the pore to the outlet of the network.

   (b) there are no continuous paths of water films in the corners from the pore to the outlet of the network.

The output from the network model is saturation-dependent capillary pressure and relative permeability functions.

Chapter 4

Data Assimilation

A mathematical model based on basic laws and principles of physics can be used to evolve the state of a system forward in time [47]. The model requires some input parameters describing the system, which are difficult to measure in practise and therefore are considered as unknowns. The correct parameters give a good match between the state estimated by the mathematical model and the available measurements of the system. This gives rise to an inverse problem, where the parameters are obtained from available measurements of the system.

Data assimilation is a powerful methodology for parameter estimation. A forecast and an analysis step are combined to produce the best estimate of the current state of the system [39, 50]. The analysis and forecasts are represented by mean and covariance of the parameters and can therefore be thought of as probability distributions. In the forecast step the state is evolved forward in time by using a mathematical model, while the analysis step tries to balance the uncertainties in the data and in the forecast. Available measurements are merged into the model and used to analyse the results from the forecast step. Uncertainty in the parameters and the model leads to uncertainty in the forecast, and the measurements are used to correct the state and the uncertainty. The result is improved modelling and a better physical understanding of the systems.

In other words, based on measurements and their uncertainties, estimates and uncertainties for the parameters are derived. By starting with some initial parameters the corresponding state is found using a mathematical model. The initial parameters are uncertain and this uncertainty is reflected in the state. By comparing the state to the measurements and taking into account their uncertainties, better estimates of the distributions of the parameters are found.

This forms the basis of the three different filters presented in this chapter. In the Kalman Filter (KF) an equation for the time evolution of the error covariance matrix is introduced for linear dynamics [39, 50, 95]. For non-linear dynamics the Extended Kalman Filter (EKF) was developed [39]. For this method the er-

ror covariance matrix is found using a linearised equation. The Kalman Filter and the Extended Kalman Filter do not work for problems with many parameters due to large computational expenses in storing the full covariance matrices. The Ensemble Kalman Filter (EnKF) was introduced as a stochastic alternative to the previous filters [18, 39]. In the Ensemble Kalman Filter the covariance matrix is represented by an ensemble of realisations. All the filters are based on the same analysis scheme, but differ in the representation of error statistics and how these evolve in time.

4.1 The analysis scheme

The analysis scheme is used to find an analysed estimate of the forecast based on available measurements in time dependent problems. Both the forecast and the measurements contain errors, and the analysis scheme uses the covariance matrices for the errors to analyse the forecast [39].

The relation between the model forecast $\boldsymbol{\Psi}^f$ and the true state $\boldsymbol{\Psi}^t$ is given by [39]

$$\boldsymbol{\Psi}^f = \boldsymbol{\Psi}^t + \boldsymbol{p}^f, \tag{4.1}$$

where $\boldsymbol{p}^f$ is the unknown error in the forecast. All variables are discretised on a numerical grid. A measurement $\boldsymbol{d}$ is related to the true state $\boldsymbol{\Psi}^t$ by

$$\boldsymbol{d} = \boldsymbol{M}\boldsymbol{\Psi}^t + \boldsymbol{\epsilon}, \tag{4.2}$$

where $\boldsymbol{\epsilon}$ is the measurement error and $\boldsymbol{M}$ is the measurement matrix, which relates the model state to the measurements. The errors in the forecast and the measurement are assumed to be independent and have zero mean, and the covariance matrices for process noise $\boldsymbol{C}^f_{\Psi\Psi}$ and measurement error $\boldsymbol{C}_{\epsilon\epsilon}$ are assumed to be known.

The analysed estimate is given by [39]

$$\boldsymbol{\Psi}^a = \boldsymbol{\Psi}^f + \boldsymbol{K}(\boldsymbol{d} - \boldsymbol{M}\boldsymbol{\Psi}^f), \tag{4.3}$$

where

$$\boldsymbol{K} = \boldsymbol{C}^f_{\Psi\Psi}\boldsymbol{M}^T(\boldsymbol{M}\boldsymbol{C}^f_{\Psi\Psi}\boldsymbol{M}^T + \boldsymbol{C}_{\epsilon\epsilon})^{-1}, \tag{4.4}$$

is the Kalman gain and $\boldsymbol{C}^f_{\Psi\Psi}$ is the forecast error covariance. The forecasted estimate $\boldsymbol{\Psi}^f$ and forecasted error covariance $\boldsymbol{C}^f_{\Psi\Psi}$ are found in the forecast step, which differ between the different filters.

The analysed error covariance is given by

$$\boldsymbol{C}^a_{\Psi\Psi} = (\boldsymbol{I} - \boldsymbol{K}\boldsymbol{M})\boldsymbol{C}^f_{\Psi\Psi}. \tag{4.5}$$

In the analysed estimate $\boldsymbol{\Psi}^a$ a weighted difference between the measurement $\boldsymbol{d}$ and the measurement prediction $\boldsymbol{M}\boldsymbol{\Psi}^f$ is added to the model forecast. The Kalman gain is the weight, constructed such that the a analysed error covariance $\boldsymbol{C}^a_{\Psi\Psi}$ is minimised.

From the definition of the Kalman gain (Eq. 4.4) some properties of the analysis scheme can be deduced [95]. The Kalman gain weights the residual more heavily as the forecast error covariance $\boldsymbol{C}_{\epsilon\epsilon}$ goes towards zero,

$$\lim_{\boldsymbol{C}_{\epsilon\epsilon}\to 0} \boldsymbol{C}^f_{\Psi\Psi}\boldsymbol{M}^T(\boldsymbol{M}\boldsymbol{C}^f_{\Psi\Psi}\boldsymbol{M}^T + \boldsymbol{C}_{\epsilon\epsilon})^{-1} = \boldsymbol{M}^{-1}. \tag{4.6}$$

Thus, the actual measurement $\boldsymbol{d}$ is trusted more when the uncertainty in the actual measurement is small. As the forecast covariance $\boldsymbol{C}^f_{\Psi\Psi}$ approaches zero, the gain $\boldsymbol{K}$ weights the residual less heavily,

$$\lim_{\boldsymbol{C}^f_{\Psi\Psi}\to 0} \boldsymbol{C}^f_{\Psi\Psi}\boldsymbol{M}^T(\boldsymbol{M}\boldsymbol{C}^f_{\Psi\Psi}\boldsymbol{M}^T + \boldsymbol{C}_{\epsilon\epsilon})^{-1} = 0. \tag{4.7}$$

The forecasted state $\boldsymbol{\Psi}^f$ is then trusted more when its uncertainty is small.

4.2 The Kalman Filter

The Kalman Filter is an efficient recursive filter that estimates the state of a dynamic system from a series of noisy measurements. It was introduced by R. E. Kalman in 1960 [50] and has later been the origin to other filters. Kalman filtering is an important topic in control theory and control systems engineering. It has been applied in many areas, particularly in navigation [48].

To use the Kalman filter to estimate the state of a process based on a sequence of noisy measurements, the process must fulfill certain conditions. It is assumed that the true state $\boldsymbol{\Psi}^t_k$ at time k is evolved from time $k-1$ by the linear stochastic difference equation

$$\boldsymbol{\Psi}^t_k = \boldsymbol{G}\boldsymbol{\Psi}^t_{k-1} + \boldsymbol{q}_{k-1}, \tag{4.8}$$

where $\boldsymbol{G}$ is a linear operator describing the dynamics of the system and $\boldsymbol{q}$ is the unknown model error. In the forecast step the analysed measurement for the state and an error covariance is computed based on the current estimate. Since the model error is unknown, it is neglected in the numerical model. The numerical model will therefore evolve according to

$$\boldsymbol{\Psi}^f_k = \boldsymbol{G}\boldsymbol{\Psi}^a_{k-1}, \tag{4.9}$$

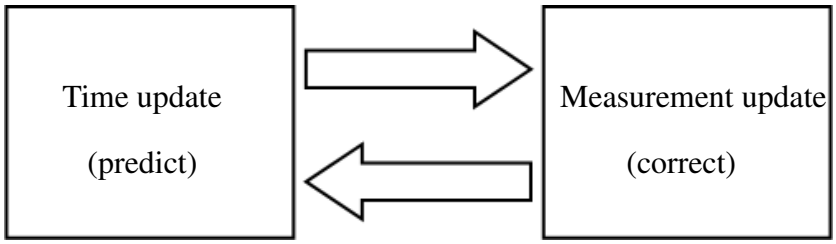

Figure 4.1: Illustration of the Kalman Filter cycle, where the time update projects the current state forward in time and the measurement update corrects the predicted estimate using a measurement at the current time.

where $\boldsymbol{\Psi}^a_{k-1}$ is the analysed estimate from Eq. (4.3). The Kalman filter introduces an equation for the time evolution of the error covariance matrix. The error covariance forecast is given by

$$\boldsymbol{C}^f_{\Psi\Psi}(t_k) = \boldsymbol{G}\boldsymbol{C}^a_{\Psi\Psi}(t_{k-1})\boldsymbol{G}^T + \boldsymbol{C}_{qq}(t_{k-1}), \tag{4.10}$$

where $\boldsymbol{C}_{qq}$ is the covariance for the model error and $\boldsymbol{C}^a_{\Psi\Psi}$ is the analysed error covariance for the forecasted estimate $\boldsymbol{\Psi}^f_k$. The forward and analysis steps are done by turns, recursively conditioning the current estimate on all the past measurements. This is illustrated in Figure 4.1.

One of the advantages with the Kalman filter is that the forward step does not require any history of measurements and estimates [50]. The Kalman filter is a recursive estimator, which means that only the estimated state from the previous time step and the current measurement are needed to compute the estimate for the current state. The Kalman filter is the optimal sequential technique for linear dynamics given that the priors are Gaussian and unbiased [39], but it has the disadvantage of not being able to handle non-linear problems.

4.3 The Extended Kalman Filter

The Extended Kalman Filter [95] is a modified version of the Kalman filter which also works for non-linear problems. It uses an approximate linearised equation to predict the error covariance.

The true state $\boldsymbol{\Psi}^t_k$ is governed by the non-linear stochastic difference equation [39]

$$\boldsymbol{\Psi}^t_k = \boldsymbol{G}(\boldsymbol{\Psi}^t_{k-1}) + \boldsymbol{q}_{k-1}, \tag{4.11}$$

where $\boldsymbol{G}(\boldsymbol{\Psi})$ is now a differentiable, non-linear model operator and $\boldsymbol{q}$ is the unknown model error. The numerical model will evolve according to

$$\boldsymbol{\Psi}_k^f = \boldsymbol{G}(\boldsymbol{\Psi}_{k-1}^t), \tag{4.12}$$

since the model error $\boldsymbol{q}$ is unknown. The expression for the covariance is similar to the expression used in the Kalman filter, but the linear operator $\boldsymbol{G}$ in Eq. (4.10) is replaced by the Jacobian of the non-linear operator $\boldsymbol{G}$. By using a Taylor expansion and neglecting terms of third and higher order the approximate error covariance equation is

$$\boldsymbol{C}_{\Psi\Psi}^f(t_k) \approx \boldsymbol{G}'_{k-1}\boldsymbol{C}_{\Psi\Psi}^a(t_{k-1})\boldsymbol{G}'^T_{k-1} + \boldsymbol{C}_{qq}(t_{k-1}), \tag{4.13}$$

where $\boldsymbol{G}'_{k-1}$ is the Jacobi matrix

$$\boldsymbol{G}'_{k-1} = \frac{\partial \boldsymbol{G}(\boldsymbol{\Psi})}{\partial \boldsymbol{\Psi}}|_{\Psi_{k-1}}. \tag{4.14}$$

This linearisation reduces the accuracy in the covariance evolution, such that the Extended Kalman Filter may fail if the non-linearities are too severe [39].

Neither the Kalman Filter nor the Extended Kalman Filter are suitable for systems with many variables due to problems with storage and updating of the covariance matrices.

4.4 The Ensemble Kalman Filter

The Ensemble Kalman Filter was introduced by Evensen in 1994 [36] and is designed to be suitable for non-linear problems with a large number of variables. The method was first used in physical oceanography [38, 51] and meteorology [5], but has later been applied in many areas, including groundwater hydrology and petroleum engineering [1, 4, 25, 61, 69, 84]. In petroleum engineering the method is used to update static and dynamic model parameters for each grid cell, as well as production data. To our knowledge, the Ensemble Kalman Filter was first applied in petroleum engineering by Lorentzen et al. [62].

The essential difference from the Kalman and Extended Kalman Filters is that the covariance matrix is replaced by a sample covariance. Thus, the distribution of the system state is represented by a collection of state vectors, also called an ensemble. The Ensemble Kalman Filter is a Monte Carlo method, such that it relies on repeated random sampling to compute a result. Monte Carlo methods are often used when it is difficult to compute an exact result with a deterministic algorithm [65]. The Ensemble Kalman Filter is often efficient compared to gradient-based methods and it also provides a reasonable estimate of the uncertainty [39].

For the Kalman filter the expression for the forecast and analysis covariance matrices are equivalent to the definitions in terms of the true state [39]

$$\begin{aligned} \boldsymbol{C}^f_{\Psi,\Psi} &= E[(\boldsymbol{\Psi}^f - \boldsymbol{\Psi}^t)(\boldsymbol{\Psi}^f - \boldsymbol{\Psi}^t)^T], \\ \boldsymbol{C}^a_{\Psi,\Psi} &= E[(\boldsymbol{\Psi}^a - \boldsymbol{\Psi}^t)(\boldsymbol{\Psi}^a - \boldsymbol{\Psi}^t)^T], \end{aligned} \tag{4.15}$$

where $E[\boldsymbol{\Psi}]$ denotes the expected value of $\boldsymbol{\Psi}$. When an ensemble of model states is introduced, it is not possible to define the covariance matrices in terms of the true state. Instead, the covariance matrices are defined in terms of the ensemble mean [39]

$$\begin{aligned} \boldsymbol{C}^f_{\Psi,\Psi} &\approx (\boldsymbol{C}^e_{\Psi,\Psi})^f = \overline{(\boldsymbol{\Psi}^f - \overline{\boldsymbol{\Psi}}^t)(\boldsymbol{\Psi}^f - \overline{\boldsymbol{\Psi}}^t)^T}, \\ \boldsymbol{C}^a_{\Psi,\Psi} &\approx (\boldsymbol{C}^e_{\Psi,\Psi})^a = \overline{(\boldsymbol{\Psi}^a - \overline{\boldsymbol{\Psi}}^t)(\boldsymbol{\Psi}^a - \overline{\boldsymbol{\Psi}}^t)^T}, \end{aligned} \tag{4.16}$$

where the overlines denote the average over the ensemble. When the ensemble size goes towards infinity, the average values converge to the expected values, such that the definition of the covariances in Eq. (4.16) will converge towards the definition in Eq. (4.15).

If the state vector has dimension n, the corresponding covariance matrix has dimension $n \times n$. It is possible to represent the covariance matrix by an ensemble of model states having the same error statistics. For large problem this is a better alternative than storage and forward integration of the error covariance matrix, as is done for the Kalman and Extended Kalman Filters.

An initial ensemble of model parameters $\boldsymbol{\Psi}$ is defined based on available information from data and statistics [39]. The states in all ensembles are linear combinations of the initial ensemble of model parameters, so it is important that prior uncertainty is represented in the initial ensemble.

An ensemble of measurements is defined by [39]

$$\boldsymbol{d}_j = \boldsymbol{d} + \boldsymbol{\epsilon}_j, \tag{4.17}$$

where $\boldsymbol{\epsilon}_j$ is the measurement error and j counts over all N ensemble members. The measurements are treated as random variables [18] distributed with mean equal to the first guess measurements and covariance equal to $\boldsymbol{C}_{\epsilon,\epsilon}$. They have zero mean, with ensemble covariance matrix defined as

$$\boldsymbol{C}^e_{\epsilon,\epsilon} = \overline{\boldsymbol{\epsilon}\boldsymbol{\epsilon}^T}. \tag{4.18}$$

In the limit of an infinite ensemble size the ensemble covariance matrix $\boldsymbol{C}^e_{\epsilon,\epsilon}$ will converge to the prescribed error covariance matrix $\boldsymbol{C}_{\epsilon,\epsilon}$ used in the Kalman Filter. This approximation introduces errors into the model, but by choosing a large enough ensemble size the errors are of less importance than the uncertainty in the true covariance $\boldsymbol{C}_{\epsilon,\epsilon}$.

In the analysis step each model state ensemble member is evolved forward in time by using similar analysis equations as earlier, but with the true covariance matrices replaced by approximate ones. In the analysis step each model state ensemble member is given by

$$\boldsymbol{\Psi}_j^a = \boldsymbol{\Psi}_j^f + \boldsymbol{K}_e(\boldsymbol{d}_j - \boldsymbol{M}\boldsymbol{\Psi}_j^f), \tag{4.19}$$

where

$$\boldsymbol{K}_e = (\boldsymbol{C}_{\Psi\Psi}^e)^f \boldsymbol{M}^T (\boldsymbol{M}(\boldsymbol{C}_{\Psi\Psi}^e)^f \boldsymbol{M}^T + \boldsymbol{C}_{\epsilon\epsilon}^e)^{-1}, \tag{4.20}$$

is called the Kalman gain.

All probability distributions involved should be approximately Gaussian. If the distributions are non-Gaussian, the estimate of the posterior probability distribution is not correct, because the analysis equations are only based on information from first and second order moments, that is mean and covariance [39]. One advantage of the Ensemble Kalman Filter is that advancing the probability distribution in time is achieved by simply advancing each member of the ensemble.

The ensemble mean

$$\overline{\boldsymbol{\Psi}}^a = \overline{\boldsymbol{\Psi}}^f + \boldsymbol{K}_e(\overline{\boldsymbol{d}} - \boldsymbol{M}\overline{\boldsymbol{\Psi}}^f). \tag{4.21}$$

is considered to be the best estimate to the true state [39]. Using an ensemble of perturbed measurements in the analysis step a new ensemble with the correct error statistics is created. The relation between the covariance matrices $(\boldsymbol{C}_{\Psi,\Psi}^e)^a$ and $(\boldsymbol{C}_{\Psi,\Psi}^e)^f$ can be expressed as

$$(\boldsymbol{C}_{\Psi,\Psi}^e)^a = (\boldsymbol{I} - \boldsymbol{K}_e\boldsymbol{M})(\boldsymbol{C}_{\Psi,\Psi}^e)^f. \tag{4.22}$$

As the ensemble size goes towards infinity both the relation between the analysed and forecasted ensemble mean and variances are identical for the Kalman Filter and the Ensemble Kalman Filter [39]. The two filters therefore give exactly the same result in the limit of infinite ensemble size for linear dynamics.

4.5 Anchoring of capillary pressure data

Two-phase capillary pressure and relative permeability data can be measured from flooding experiments in a laboratory, while it is difficult to obtain three-phase data. A simulation of the experiments could be done with a network model if the input parameters were known. The input parameters describe the geometry and wettability of the core and the fluid properties. The idea is to find the input parameters which give a match between the two-phase capillary pressure curves produced by the network model and the experimental measurements [64, 88]. Afterwards, the

same input parameters are used to predict three-phase capillary pressures for optional saturations with the network model. This approach is based on the assumption that the three-phase capillary pressures limit to two-phase capillary pressures as one of the phase saturations goes towards zero. The weakness of this strategy is that parameters that have a large effect in three-phase flow, but not in two-phase flow, are difficult to find.

We have used measurements for two-phase capillary pressure between mercury and nitrogen, oil and water, and gas and oil. The data are obtained from centrifuge experiments on three cores from the North Sea, where mercury is injected into a core plug filled with nitrogen, water is injected into a core filled with oil and residual water, and gas is injected into a core plug filled with oil and residual water. The cores are from the same area and are assumed to have the same properties.

The network model has about 25 parameters. The fluid properties are known, while the geometry and wettability parameters are considered to be the unknown parameters. Based on wettability tests it is known that the cores are mixed-wet large.

First we tried to find out which effect each parameter had on the capillary pressure curve by modifying one parameter at the time. Because of the large number of parameters, it was only done for the parameters we thought had the largest effect on the capillary pressure curves. When using three different values for each parameter, the effect on the capillary pressure curves was not clear for many of the parameters. This was not unexpected, since the network model has a complex behaviour. A result is that manually anchoring of two-phase capillary pressure curves from the network model to experimental data [30] is very time consuming.

To automate the anchoring we considered using gradient methods [71]. First we had to define an objective function which tells how close the capillary pressure curves from the network model are to the measurements. This is not straight forward, since the capillary pressure goes towards infinity at the asymptotes. A gradient defining the change in the objective function with respect to a parameter is found by running the network model for two different values of the parameter. Because of the high number of unknowns it is very time consuming to estimate gradients with respect to all parameters. In addition, the gradients are often zero, because of threshold effects in the network. There are no clear trends in the parameters and this would most likely lead us to a local minimum instead of a global.

The next step was to try stochastic methods, and the Ensemble Kalman Filter was used to assimilate capillary pressure data for the anchoring problem. Earlier, the Ensemble Kalman Filter has been used in time-dependent problems to update a model continuously. Capillary pressure functions are not time-dependent, such that the method had to be adjusted to work on the anchoring problem. This is

solved by considering the saturation as the time variable in the filter. The capillary pressure data are the measurements, which are available for different saturations. The first measurement is the capillary pressure for the lowest saturation of the injected fluid and as the saturation increases we get new capillary pressure measurements. The network model is considered as a black box, which takes in input parameters and gives out capillary pressure for a specified saturation.

Some modifications had to be done to adapt the Ensemble Kalman Filter to the anchoring problem. Most parameters in the network model have to be located between lower and upper limits a and b, respectively, because values outside this interval are not meaningful. If we do not have any information about the parameters, no values within the interval are more likely than others, such that it is natural to use a uniform probability distribution. The Ensemble Kalman Filter is based on the assumption that all probability distributions are normal, such that a transformation between the uniform to the normal distributions is necessary. This is done by using cumulative distributions, which gives the probability that a parameter value is lower than a given value. The uniform distribution is transformed to normal distribution which has the same cumulative distribution, and the other way around. All calculations in the EnKF algorithm is done with distributed normally parameters, while a call to the network simulator is done with uniformly distributed parameters as input.

The first ensemble of parameters is made based on the mean and the variance for the parameters. For the uniform distribution the mean is the mean of the interval (a, b) and the variance is $\frac{(b-a)^2}{12}$. For the measurements we assume that 90 percent of the measurements contain less then 10 percent error and that the error follows a normal distribution. This leads to a variance of about 0.35 percent of the measured value. We assume that there is no correlation between the measurements, such that the covariance matrix is a diagonal matrix with the variance for each parameter along the diagonal [94].

The capillary pressure curves have asymptotic behaviour near residual saturations. Thus, for a very small change in saturation the capillary pressure change substantially. To measure how well the capillary pressure matches the measurement in the asymptote, the saturation where the asymptote is placed is evaluated instead of the capillary pressure value.

To be able to evaluate the accuracy of the parameters found by the Ensemble Kalman filter we matched capillary pressure curves from a synthetic case made by running the network model for a set of input parameters. This also allow us to vary the number of unknown input parameters to find in the matching. The conclusion was that most parameters were close to the true ones, even when all parameters were considered as unknowns. Details and results are included in Paper D.

Chapter 5

Summary of Papers

Five papers are included in the thesis. Three of them are accepted for journal publication and two are presented on conferences. This chapter contains short summaries and main conclusions for the included papers.

As all the papers are collaborative work, some remarks about my contribution are necessary. The work in papers A-C is based on theory in an existing paper [90]. My contribution is implementation and numerical simulations, mainly performed at the Heriot Watt University under the supervision of Rink van Dijke and Sebastian Geiger. In paper D the Ensemble Kalman Filter was adapted to work on a process dependent on saturation instead of time. I have done the implementation and numerical simulations in cooperation with Roland Kaufmann. In Paper E an existing meshing algorithm [73] is extended to domains with internal boundaries. Also in this paper I have done the implementation and testing of the algorithm together with Roland Kaufmann.

5.1 Paper A

Title: Consistent Capillary Pressure and Relative Permeability for Mixed-wet Systems in Macroscopic Three-phase Flow Simulation

Authors: R. Holm, M. I. J. van Dijke, S. Geiger and M. Espedal

Presented at 11^{th} European Conference on the Mathematics of Oil Recovery*, 8 - 11 September 2008, Bergen, Norway*

The capillary bundle model was used to produce consistent three-phase capillary pressure and relative permeability functions for water-wet and oil-wet wettability states. Simulations were performed on the pore-scale and the continuum-

scale by injecting gas into an initially oil- and water-filled medium. On the continuum-scale the effect of viscous forces were studied by using three different gas viscosities and the effect of capillary forces were studied by performing simulations both with and without capillary pressures. By studying the saturation paths in the ternary diagram the pore-scale and continuum-scale simulations were compared.

Main results of the paper

- No exact agreement between saturation paths for the pore-scale and continuum-scale models.
- Including capillary pressures results in smoother saturation paths.
- Decreasing the gas viscosity has a similar effect as including capillary pressures.

5.2 Paper B

Title: Three-phase flow modelling using pore-scale capillary pressures and relative permeabilities for mixed-wet systems

Authors: R. Holm, M. I. J. van Dijke, S. Geiger and M. Espedal

Presented at 10^{th} Wettability Conference*, 27 - 28 October 2008, Abu Dhabi, UAE*

This paper is an extension of the work in Paper A. The same models were used, but with flow functions for four different wettability state and two different values of the gas-oil interfacial tensions. Also in this work gas is injected into an oil- and water-filled medium, and on the continuum-scale simulations are performed both with and without capillary pressures.

Main results of the paper

- In oil-wet cases mainly water is displaced first, while in water-wet cases mainly oil is displaced first.
- The weakly wetted and mixed-wet cases give paths in between the strongly oil and water-wet cases.
- The lower gas-oil interfacial tension leads to slightly more water displaced during the first part of the displacement.

5.3 Paper C

Title: Three-phase flow modelling using pore-scale capillary pressures and relative permeabilities for mixed-wet media at the continuum-scale

Authors: R. Holm, M. I. J. van Dijke, and S. Geiger

Accepted for publication in Transport in Porous Media

This paper is an extension of the work in Paper B, but instead of varying the gas-oil interfacial tension, three different initial saturations are used.

Main results of the paper

- Mixed-wet cases show water-wet behaviour for low initial water saturations and oil-wet behaviour for high initial water saturations.
- The effect of wettability is large also when capillary pressures are neglected.

5.4 Paper D

Title: Constructing three-phase capillary pressure functions by parameter matching using a modified Ensemble Kalman Filter

Authors: R. Holm, R. Kaufmann, E. I. Dale, S. Aanonsen, G. E. Fladmark, M. Espedal and A. Skauge

Accepted for publication in Communications in Computational Physics*, Volume 6, Number 1, pages 24-48, July 2009*

In this paper a network model is used to predict three-phase capillary pressures. The network model has about 20 unknown input parameters, describing geometry and wettability of the network. From laboratory experiments on core plugs there exist measurements for two-phase capillary pressures between mercury and nitrogen, oil and water, and oil and gas. We tried to recreate the experiments with a network model and chose the input parameters that give the best match between the experimental and simulated capillary pressures. This is done by a modified Ensemble Kalman filter, which uses a stochastic approach to find the best parameters. Earlier, the Ensemble Kalman Filter has only been applied to time dependent problems, such that some modifications were necessary in order

to make the method work for this problem. The accuracy of the method was determined by matching capillary pressure curves which were made by running the network model for a set of parameters. Afterwards, the network model is started from different initial saturations to create capillary pressure data following different saturation paths that together covers the three-phase saturation space. These three-phase capillary pressure data can be used as input to a reservoir simulator.

Main results of the paper

- Most parameter values were close to the correct ones.
- Parameters that only have a large impact in three-phase flow are difficult to match.

5.5 Paper E

Title: Meshing of domains with complex internal geometries

Authors: R. Holm, R. Kaufmann, B.-O. Heimsund, E. Øian and M. S. Espedal

Published in Numerical Linear Algebra with Applications*, Volume 13, pages 717-731, November 2006*

This paper presents a meshing algorithm for domains with internal boundaries, such as fractures. It is an extension of the triangulation algorithm presented by Persson and Strang [73]. Equilateral triangles are beneficial for a finite volume discretization, as fluid flow between elements of very different size is only possible at small time steps.

Main results of the paper

- The resulting triangulation matches all boundaries and the triangles are all nearly equilateral.
- Both the element quality and simulation performance are better than for meshes produced with the well regarded Triangle program [80].

Bibliography

[1] S. I. Aanonsen, G. Nævdal, D. S. Oliver, A. C. Reynolds, and B. Valles. Ensemble Kalman Filter to petroleum engineering. To appear in SPE J., 2009.

[2] R. A. Adams. *Calculus*. Addison Wesley, 1999.

[3] H. S. Al-Hadhrami and M. J. Blunt. Thermally induced wettability alteration to improve oil recovery in fractured reservoirs. *SPE Reserv. Eval. Eng.*, 4(3):179–186, 2001.

[4] A. Almendral-Vazquez and A. R. Syversveen. The Ensemble Kalman Filter - theory and applications in oil industry. Technical report, Norsk Regnesentral, 2006.

[5] J. L. Anderson, B. Wyman, S. Zhang, and T. Hoar. Assimilation of surface pressure observations using an ensemble filter in an idealized global atmospheric prediction system. *J. Atmos. Sci.*, 62(8):2925–2938, 2005.

[6] T. Austad, S. Strand, M. V. Madland, T. Puntervold, and R. I. Korsnes. Seawater in chalk: An EOR and compaction fluid. *SPE Reserv. Eval. Eng.*, 11(4):648–654, August 2008. SPE 118431.

[7] K. Aziz. *Petroleum Reservoir Simulation*. Applied science publishers ltd, 1979.

[8] L. E. Baker. Three-phase relative permeability correlations. In *Enhanced Oil Recovery Symposium*, Tulsa, OK, April 17-20 1988. SPE.

[9] F. E. Bartell and H. J. Osterhof. Determination of the wettability of a solid by a liquid. *Ind. Eng. Chem.*, 19(11):1277–1280, 1927.

[10] D. B. Bennion, F. B. Thomas, and R. F. Bietz. Hysteretic relative permeability effects and reservoir conformance - an overview. Technical report, Hycal Energy Research Laboratories Ltd., 1996.

[11] M. J. Blunt. An empirical model for three-phase relative permeability. *SPE J.*, 5(4):435–445, December 2000.

[12] M. J. Blunt, M. D. Jackson, M. Piri, and P. H. Valvatne. Detailed physics, predictive capabilities and macroscopic consequences for pore-network models of multphase flow. *Adv. Water Resour.*, 25:1069–1089, 2002.

[13] M. J. Blunt, M. J. King, and H. Scher. Simulation and theory of two-phase flow in porous media. *Phys. Rev. A*, 46(12):7680–7702, 1992.

[14] M. J. Blunt and P. King. Relative permeabilities from two- and three-dimensional pore-scale network modelling. *Transp. Porous Med.*, 6:407–433, 1991.

[15] S. R. Broadbent and J. M. Hammersley. Percolation processes. *Math. Proc. Cambridge Philos. Soc.*, 53(3):629–645, 1957.

[16] R. H. Brooks and A. T. Corey. Hydraulic properties of porous media. *Hydrol. Pap.*, 3, 1964.

[17] N. T. Burdine. Relative permeability calculations from pore-size distribution data. *T. SPE AIME*, 198:71–78, 1953.

[18] G. Burgers, P. J. van Leeuwen, and G. Evensen. Analysis scheme in the Ensemble Kalman Filter. *Mon. Weather. Rev.*, 126:1719–1724, June 1998.

[19] F. M. Carlson. Simulation of relative permeability hysteresis to the non-wetting phase. In *SPE Annual Technical Conference and Exhibition*, 4-7 October 1981.

[20] M. Carlson. *Practical Reservoir Simulation*. Penn Well Corporation, 2003.

[21] P. C. Carman. Fluid flow through granular beds. *Trans. Inst. Chem. Eng.*, 15:150–156, 1937.

[22] P. C. Carman. *Flow of Gases through Porous Media*. Butterworths Scientific Publications, 1956.

[23] M. A. Celia, P. C. Reeves, and L. A. Ferrand. Recent advances in pore scale models for multiphase flow. *Rev. Geophys. Suppl.*, 33:1049–1057, 1995.

[24] I. Chatzis, N. R. Morrow, and H. T. Lim. Magnitude and detailed structure of residual oil saturation. *SPE J.*, 23(2):311–326, April 1983.

[25] Y. Chen, D. S. Oliver, and D. Zhang. Efficient ensemble-based closed-loop production optimization. In *SPE/DOE Symposium on Improved Oil Recovery*, Tulsa, Oklahoma, USA, 20-23 April 2008.

[26] Z. Chen, G. Huan, and Y. Ma. *Computational Methods for Multiphase Flows in Porous Media*. Siam, 2006.

[27] J. R. Christensen, E. H. Stenby, and A. Skauge. Review of WAG field experience. *SPE Reserv. Eval. Eng.*, 4(2):97–106, April 2001. SPE 71203.

[28] A. T. Corey, C. H. Rathjens, J. H. Henderson, and M. R. J. Wyllie. Three-phase relative permeability. *Trans. AIME*, 207:349–351, 1956.

[29] E. I. Dale. *Modelling of immiscible WAG with emphasis on the effect of capillary pressure*. PhD thesis, University of Bergen, Norway, 2008.

[30] E. I. Dale and A. Skauge. Features concerning capillary pressure and the effect on two-phase and three-phase flow. In *Timing of IOR to Maximise Production Rates and Ultimate Recovery*, Cairo, Egypt, 22–24. April 2007. International EAGE - IOR symposium.

[31] H. Darcy. Les Fontaines Publiques de la Ville de Dijon, 1856. Dalmont, Paris.

[32] P.-G. de Gennes, F. Brochard-Wyart, and D. Quéré. *Capillary and Wetting Phenomena – Drops, Bubbles, Pearls, Waves*. Springer, 2002.

[33] M. Delshad and G. A. Pope. Comparison of the three-phase oil relative permeability models. *Transp. Porous Med.*, 4:59–83, 1989.

[34] L. J. Durlofsky. Coarse scale models of two phase flow in heterogeneous reservoirs: volume averaged equations and their relationship to existing upscaling techniques. *Computat. Geosci.*, 2:73–92, 1998.

[35] L. C. Evans. *Partial Differential Equations*. American Mathematical Society, 2002.

[36] G. Evensen. Sequential data assimilation with a nonlinear quasi-geostrophic model using Monte Carlo methods to forecast error statistics. *J. Geophys. Res.*, 99(C5):10143–10162, May 1994.

[37] G. Evensen. The Ensemble Kalman Filter: theoretical formulation and practical implementation. *Ocean Dynam.*, 53(4):343–367, 2003.

[38] G. Evensen. Sampling strategies and square root analysis schemes for the EnKF. *Ocean Dynam.*, 54:539–560, 2004.

[39] G. Evensen. *Data Assimilation, The Ensemble Kalman Filter*. Springer, 2007.

[40] I. Fatt. The network model of porous media. *Petroleum Transactions, AIME*, 207:144–181, 1956.

[41] F. J. Fayers and J. D. Matthews. Evaluation of normalized Stone's methods for estimating three-phase relative permeabilities. *SPE J.*, 24(2):224–232, April 1984.

[42] D. H. Fenwick and M. J. Blunt. Three-dimensional modeling of three phase imbibition and drainage. *Adv. Water Resour.*, 21(2):121–143, March 1998.

[43] M. G. Gerritsen and L. J. Durlofsky. Modeling fluid flow in oil reservoirs. *Annu. Rev. Fluid Mech.*, 37:211–238, 2005.

[44] A. A. Heiba, M. Sahimi, L. E. Scriven, and H. T. Davis. Percolation theory of two-phase relative permeability. *SPE J.*, 7(1):123–132, 1992.

[45] J. O. Helland and S. M. Skjæveland. Three-phase capillary pressure correlation for mixed-wet reservoirs. In *SPE International Petroleum Conference*, Puebla Pue., Mexico, 7-9 November 2004. SPE 92057.

[46] J. O. Helland and S. M. Skjæveland. Physically-based capillary pressure correlation for mixed-wet reservoirs from a bundle-of-tubes model. *SPE J.*, 11(2):171–180, 2006.

[47] R. Helmig. *Multiphase Flow and Transport Processes in the Subsurface: A Contribution to the Modeling of Hydrosystems*. Springer, 1997.

[48] C. Hu, W. Chen, Y. Chen, and D. Liu. Adaptive Kalman filtering for vehicle navigation. *Journal of GPS*, 2(1):42–47, 2003.

[49] M.-H. Hui and M. J. Blunt. Effects of wettability on three-phase flow in porous media. *J. Phys. Chem.*, 104:3833–3845, 2000.

[50] R. E. Kalman. A new approach to linear filtering and prediction problems. *J. Basic. Eng. - T. ASME*, 82 (Series D):35–45, 1960.

[51] J. D. Kepert. On ensemble representation of the observation-error covariance in the Ensemble Kalman filter. *Ocean Dynam.*, 54:561–569, 2004.

[52] J. E. Killough. Reservoir simulation with history-dependent saturation functions. *Trans. AIME*, 261:37–48, 1976.

[53] A. Kjosavik, J. K. Ringen, and S. M. Skjæveland. Relative permeability correlation for mixed-wet reservoirs. *SPE J.*, 2000. SPE 59314.

[54] C. S. Land. Calculation of imbibition relative permeability for two- and three-phase flow from rock properties. *SPE J.*, 8(2):149–156, 1968.

[55] C. S. Land. Comparison of calculated with experimental imbibition relative permeability. *SPE J.*, 11(4):419–425, 1971.

[56] P. S. D. Laplace. *Mechanique Celeste, Supplement to Book 10*. 1806.

[57] J. A. Larsen and A. Skauge. Simulation of the immiscible WAG process using cycle-dependent three-phase relative permeabilities. In *SPE Annual Technical Conference and Exhibition*, Houston, Texas, 3-6 October 1999. SPE 56475.

[58] R. G. Larson, L. E. Scriven, and H. T. Davis. Percolation theory of two phase flow in porous media. *Chem. Eng. Sci.*, 36(1):57–73, 1981.

[59] M. C. Leverett. Capillary behavior in porous solids. *Petroleum Transactions, AIME*, 142:152–169, 1941.

[60] J. R. Lien and G. Løvhøiden. *Generell fysikk for universiteter og høgskoler*. Universitetsforlaget, 2001.

[61] N. Liu and D. S. Oliver. Ensemble Kalman filter for automatic history matching of geologic facies. *J. Petrol. Sci. Eng.*, 47:147–161, 2005.

[62] R. J. Lorentzen, K. K. Fjelde, J. Frøyen, A. C. V. M. Lage, G. Nævdal, and E. H. Vefring. Underbalanced drilling: Real time data interpretation and decision support. In *SPE/IADC Drilling Conference*, Amsterdam, Netherlands, 27 February - 1 March 2001.

[63] A. E. Lothe, R. H. Gabrielsen, N. B. Hagen, and B. T. Larsen. An experimental study of the texture of deformation bands: effects on the porosity and permeability of sandstones. *Petrol. Geosci.*, 8:195–207, 2002.

[64] S. McDougall, J. Cruickshank, and K. S. Sorbie. Anchoring methodologies for pore-scale network models: Application to relative permeability and capillary pressure prediction. In *Proceedings of the International Symposium of the Society of Core Analysts*, Edinburgh, Scotland, 1719 September 2001. SCA 2001-15.

[65] N. Metropolis and S. Ulam. The Monte Carlo method. *J Am Stat Assoc*, 44(247):335–341, September 1949.

[66] R. Millman and G. Parker. *Elements if Differential Geometry*. Prentice-Hall, 1977.

[67] Y. Mualem. A new model for predicting the hydraulic conductivity of unsaturated porous media. *Water Resour. Res.*, 12:513–522, 1976.

[68] M. Muskat, R. D. Wyckoff, H. G. Botset, and M. W. Meres. Flow of gas-liquid mixtures through sands. *T. SPE AIME*, 123:69–82, 1937.

[69] G. Nævdal, L. M. Johnsen, S. I. Aanonsen, and E. H. Vefring. Reservoir monitoring and continuous model updating using Ensemble Kalman Filter. *SPE J.*, March 2005.

[70] I. Neuweiler and H.-J. Vogel. Upscaling for unsaturated flow for non-gaussian heterogeneous porous media. *Water Resour. Res.*, 43:1–15, 2007.

[71] J. Nocedal and S. J. Wright. *Numerical Optimization*. Springer, 2nd edition, 2006. ISBN: 03 87 30 30 30.

[72] E. Øian. *Modeling of Flow in Faulted and Fractured Media*. PhD thesis, Department of Mathematics, University of Bergen, March 2004.

[73] P.-O. Persson and G. Strang. A simple mesh generator in MATLAB. *SIAM Rev.*, 46(2):329–345, June 2004.

[74] Ø. Pettersen. Grunnkurs i reservoarmekanikk, 1990.

[75] M. Piri and M. J. Blunt. Three-dimensional mixed-wet random pore-scale network modeling of two- and three-phase flow in porous media. i. model description. *Phys. Rev. E*, 71(026301):1–30, 2005.

[76] M. Piri and M. J. Blunt. Three-dimensional mixed-wet random pore-scale network modeling of two- and three-phase flow in porous media. ii. results. *Phys. Rev. E*, 71(026301):1–11, 2005.

[77] W. R. Purcell. Capillary pressures - their measurement using mercury and the calculation of permeability therefrom. *Trans. AIME*, 186:39–48, 1949.

[78] L. A. Richards. Capillary conduction of liquids through porous mediums. *J. Appl. Phys.*, 1:318–333, 1931.

[79] R. C. Selley. *Elements of Petroleum Geology*. Academic Press, 1998.

[80] J. R. Shewchuk. Triangle: Engineering a 2D Quality Mesh Generator and Delaunay Triangulator. In M. C. Lin and D. Manocha, editors, *Applied Computational Geometry: Towards Geometric Engineering*, volume 1148 of *Lecture Notes in Computer Science*, pages 203–222. Springer-Verlag, May 1996. From the First ACM Workshop on Applied Computational Geometry.

[81] A. Skauge and E. A. Berg. Immiscible WAG injection in the Fensfjord formation of the Brage Oil field. In *9th European Symposium on Improved Oil Recovery*, The Hague, October 20-22 1997. EAGE.

[82] A. Skauge and J. Å. Stensen. Review of WAG field experience. In *Modern Challenges in Oil Recovery*, Russia, Moscow, Gubkin University, 2003. 1^{st} International Conference and Exhibition.

[83] S. M. Skjæveland, L. M. Siqveland, A. Kjosavik, W. L. Hammervold Thomas, and G. A. Virnovsky. Capillary pressure correlation for mixed-wet reservoirs. *SPE J.*, 3(1):60–67, 2000.

[84] J.-A. Skjervheim. *Continuous Updating of a Coupled Reservoir-Seismic Model Using an Ensemble Kalman Filter Technique*. PhD thesis, Department of Mathematics, University of Bergen, Norway, January 2007.

[85] K. S. Sorbie and M. I. J. van Dijke. Fundamentals of three-phase flow in porous media of heterogeneous wettability. Institute of Petroleum Engineering, Heriot-Watt University, Edinburgh, Scotland, September 2004.

[86] H. L. Stone. Probability model for estimating three-phase relative permeability. *Trans. SPE AIME*, 249:214–218, 1970.

[87] H. L. Stone. Estimation of three-phase relative permeability and residual oil data. *J. Can. Petrol. Technol.*, 12(4):53–61, February 1973.

[88] D. S. Svirsky, M. I. J. van Dijke, and K. S. Sorbie. Prediction of three-phase relative permeabilities using a pore-scale network model anchored to two-phase data. *SPE Reserv. Eval. Eng.*, 10(5):527–538, 2007.

[89] D. Tiab and E. C. Donaldson. *Petrophysics - Theory and Practice of Measuring Reservoir Rock and Fluid Transport Properties*. Gulf Professional Publishing, 2004.

[90] M. I. J. van Dijke and K. S. Sorbie. An analysis of three-phase pore occupancies and relative permeabilities in porous media with variable wettability. *Transp. Porous Med.*, 48:159–185, 2002.

[91] M. I. J. van Dijke and K. S. Sorbie. Pore-scale network model for three-phase flow in mixed-wet porous media. *Phys. Rev. E*, 66(4):046302.1–046302.14, 2002.

[92] M. I. J. van Dijke, K. S. Sorbie, and S. R. McDougall. Saturation-dependencies of three-phase relative permeabilities in mixed-wet and fractionally wet systems. *Adv. Water Resour.*, 24:365–384, 2001.

[93] M. T. van Genuchten. A closed-form equation for predicting the hydraulic conductivity of unsaturated soils. *Soil. Sci. Soc. Am. J.*, 44:892–898, 1980.

[94] R. E. Walpole, R. H. Myers, S. L. Myers, and K. Ye. *Probability & Statistics for Engineers & Scientists*. Prentice-Hall, 2002.

[95] G. Welch and G. Bishop. An introduction to the Kalman Filter. Technical report, Department of Computer Science, 1995.

[96] S. Whitaker. Flow in porous media I: A theoretical derivation of Darcy's law. *Transp. Porous Med.*, 1:3–25, 1986.

[97] S. Whitaker. Flow in porous media II: The governing equations for immiscible, two-phase flow. *Transp. Porous Med.*, 1:105–125, 1986.

[98] S. Whitaker. *The Method of Volume Averaging*. Kluwer Academic Publishers, 1999.

[99] D. Wilkinson and J. F. Willemsen. Invasion percolation: a new form of percolation theory. *J. Phys. A*, 16:3365–3376, 1983.

[100] T. Young. An essay on the cohesion of fluids. *Philos. Trans. R. Soc. London*, 95:65–87, 1805.